

University of Nebraska - Lincoln

DigitalCommons@University of Nebraska - Lincoln

---

Engineering Mechanics Dissertations & Theses

Mechanical & Materials Engineering,  
Department of

---

Summer 7-2012

## Propagation of Ultrasound through Freshly Excised Human Calvarium

Armando Garcia Noguera

University of Nebraska – Lincoln, aagn17@gmail.com

Follow this and additional works at: <https://digitalcommons.unl.edu/engmechdiss>



Part of the [Biomaterials Commons](#), [Engineering Mechanics Commons](#), [Engineering Physics Commons](#), [Mechanical Engineering Commons](#), and the [Mechanics of Materials Commons](#)

---

Garcia Noguera, Armando, "Propagation of Ultrasound through Freshly Excised Human Calvarium" (2012). *Engineering Mechanics Dissertations & Theses*. 31.  
<https://digitalcommons.unl.edu/engmechdiss/31>

This Article is brought to you for free and open access by the Mechanical & Materials Engineering, Department of at DigitalCommons@University of Nebraska - Lincoln. It has been accepted for inclusion in Engineering Mechanics Dissertations & Theses by an authorized administrator of DigitalCommons@University of Nebraska - Lincoln.

Propagation of Ultrasound through Freshly Excised Human Calvarium

By

Armando Garcia Noguera

A THESIS

Presented to the Faculty of

The Graduate College at the University of Nebraska

In Partial Fulfillment of Requirements

For the Degree of Master of Science

Major: Engineering Mechanics

Under the Supervision of Professor Joseph A. Turner

Lincoln, Nebraska

July, 2012

# Propagation of Ultrasound through Freshly Excised Human Calvarium

Armando Garcia Noguera, M.S

University of Nebraska, 2012

Adviser: Joseph A. Turner

The propagation of ultrasound through complex biological media, such as the human calvarium, poses a great challenge for modern medicine. Several ultrasonic techniques commonly used for treatment and diagnosis in most of the human body are still difficult to apply to the human brain, in part, because of the properties of the skull. Moreover, an understanding of the biomechanics of transcranial ultrasound may provide needed insight into the problem of blast wave induced traumatic brain injury (TBI). In the present study, the spatial variability of ultrasonic properties was evaluated for relevant frequencies of 0.5, 1, and 2.25 MHz. A total of eighteen specimens from four donors were tested using a through-transmission configuration. With the aid of a two interface model, the ultrasonic attenuation coefficient was determined from the total energy loss at various locations on the specimens. With the same setup, speed of sound through the bone layer at the same locations was also determined. Mean volumetric densities at various locations on the samples were determined from computed tomography images. The results show good correlation between attenuation and volumetric density, particularly for the higher frequencies. In addition, the spatial variability of the attenuation, within a single person and with

respect to different people, was found to be much larger than expected. These results are anticipated to have a major impact on transcranial biomedical research.

# Aknowledgments

I would like to acknowledge that without the advisory and support of Dr. Joseph Turner and the excellent facilities at the Department of Mechanical and Materials Engineering, this project would have not been possible. I would also like to express my gratefulness to Dr. Mehrdad Negahban for giving me the opportunity of becoming a graduate student of this prestigious College of Engineering, and for his important influence in my formation. Thanks to the members of the review committee Dr. Negahban and Dr. Feng for providing invaluable comments and suggestions about this work. I also want to extend my gratitude to every member of Dr. Turner's research team. They have made this experience even more stimulating with their advice, support and friendship. The contributions of Dr. Robert Salzar and the University of Virginia are gratefully acknowledged. My gratitude is also extended to the Army Research Office for posing their trust in this research.

Finally, especial appreciation is to the endless support of my family and fiancée. They have been key to all the accomplishments in my short career. This work is dedicated in particular to my parents and siblings. They deserve to share part of this success with me.

# Contents

<b>List of Figures.....</b>	<b>vii</b>
<b>List of Tables.....</b>	<b>xi</b>
<b>Chapter 1 .....</b>	<b>1</b>
<b>Introduction.....</b>	<b>1</b>
<b>Chapter 2 .....</b>	<b>5</b>
<b>Background .....</b>	<b>5</b>
2.1. Longitudinal Waves .....	5
2.2. Shear Waves.....	6
2.3. Critical Angle.....	7
2.4. Ultrasonic Transducers .....	9
2.5. Ultrasound for NDT and Material Characterization .....	12
2.6. Measurement Configurations.....	13
2.7. A and C Data Acquisition Modes .....	15
<b>Chapter 3 .....</b>	<b>17</b>
<b>Calvarium Specimens .....</b>	<b>17</b>
3.1. Human Calvarium.....	17
3.2. Excision of Calvarium Specimens .....	19
<b>Chapter 4 .....</b>	<b>23</b>

<b>Density from Computed Tomography .....</b>	<b>23</b>
4.1. Computed Tomography in Biomaterials .....	24
4.2. Phantom Materials .....	25
4.3. Conversion of Hounsfield Units to Real Density .....	28
4.4. Mean volumetric Density Determination.....	34
<b>Chapter 5 .....</b>	<b>36</b>
<b>Propagation of Ultrasound through Human Calvarium .....</b>	<b>36</b>
5.1. Equipment .....	36
5.2. Experimental Procedure .....	39
5.3. Ultrasound for Thickness and Curvature Measurements .....	42
5.4. Measurement of ultrasound properties.....	47
<b>Chapter 6 .....</b>	<b>56</b>
<b>Results and Discussion .....</b>	<b>56</b>
6.1. Wave speed .....	56
6.2. Attenuation coefficient.....	58
<b>Chapter 7 .....</b>	<b>56</b>
<b>Conclusions and Future Work .....</b>	<b>70</b>

# List of Figures

Figure 1. When longitudinal waves propagate through a material, the particles execute an oscillating motion parallel to .....	7
Figure 2. The behavior of incident plane waves at the interface of two media at an oblique angle can be modeled as shown following Snell's generalized law. ....	8
Figure 3. The basic elements of an ultrasound transducer are: housing for protection of internal components, circuitry to input .....	11
Figure 4. Shape and intensity of the beam vary at different distances from the face. Near field: highly fluctuating intensity .....	12
Figure 5. A: In pulse-echo configuration a single transducer is employed as both the source and the receiver. Reflections from.....	14
Figure 6. Typical UTWin® display showing both A-mode and C-mode. At the top of the image the received amplitude-modulated .....	16
Figure 7. The human skull is composed by several irregularly shaped bones including the lower mandible. The frontal, two parietal.....	19
Figure 8. Rectangular shaped fragments were excised from frontal, parietal, temporal, and occipital regions of the heads. Samples were.....	21
Figure 9. A 3D CT image is reconstructed from several 2D x-rays. These 2D x-rays are taken at slightly different angles around the .....	24
Figure 10. Density measurements were performed with a Toledo Mettler AT201 electronic analytical semimicro balance.....	27



Figure 11. Calvarium specimens were CT scanned using a Light Speed Plus 16-Slice CT scanner at the BryanLGH Medical Center-West.....	29
Figure 12. With the tool for density determination, densities on the phantom areas of the images at different depths were determined .....	31
Figure 13. Correlation curves were determined for each session from pixel data in Hounsfield units of the reference materials in the CT .....	32
Figure 14. The CT images used in the present work were circular images padded with values of $-2000$ before slope and intercept correction.....	33
Figure 15. Ps: pixel size. Ss: step size. Mean density values were volumetrically determined from CT images. An algorithm written in .....	35
Figure 16. Volumetric average densities were determined at various locations on the CT images. From this matrix the densities of a region.....	35
Figure 17. Multi-transducer fixture made with t-slotted framing allowed the placement of transducer holders and sound absorbing .....	39
Figure 18. Ultrasound evaluation was performed in a Mistras immersion system: Motion control system, water purification system.....	41
Figure 19. Thickness at different locations on the specimens were determined using a cross-correlation function between reference echo.....	43
Figure 20. Values $tcc1$ and $tcc2$ are the time of flight differences between reference and specimen echo pulses. Echo1: reflection from.....	44
Figure 21. Transmission coefficient is small at normal incidence and remains almost constant until incidence at nearly the first critical angle.....	46

Figure 22. Surface profile of fragment I-T was reconstructed using the echo data on the convex side of the fragment. A polynomial surface .....	47
Figure 23. A: Reference waveform is delayed with respect to sample waveform. The delay is the result of a higher speed of propagation.....	49
Figure 24. Attenuation coefficient in dB/cm and its frequency dependence has been determined in previous research for some biological .....	53
Figure 25. When the ultrasound beam encounters the interface water-bone, part of the energy is reflected back to the transducer. Then, part .....	55
Figure 26. Procedure for calculating attenuation coefficient using 0.5 MHz signal through the calvarium samples. A: Reference pulse.....	59
Figure 27. Procedure for calculating attenuation coefficient using 1 MHz signal through the calvarium samples. A: Reference pulse.....	60
Figure 28. Procedure for calculating attenuation coefficient using 2.25 MHz signal through the calvarium samples. A: Reference pulse.....	60
Figure 29. 2-D color images show regions of high and low attenuation for the five fragments excised from head I at 0.5 MHz.....	65
Figure 30. Histograms computed from attenuation coefficient data show the spatial variability of attenuation values for the five fragments .....	65
Figure 31. 2-D color images show regions of high and low attenuation for the five fragments excised from head I at 1 MHz.....	66
Figure 32. Histograms computed from attenuation coefficient data show the spatial variability of attenuation values for the five fragments .....	66

Figure 33. 2-D color images show regions of high and low attenuation for the five fragments excised from head I at 2.25 MHz.....	67
Figure 34. Histograms computed from attenuation coefficient data show the spatial variability of attenuation values for the five fragments.....	67
Figure 35. Correlation between mean volumetric density and mean attenuation coefficient for all fragments at frequencies of 0.5, 1 and. ....	69

# List of Tables

Table 1. Relevant information about the calvarium donors.....	21
Table 2. Density of bone mineral and compact bone ashing previously reported (Rustgi et al., 1980).....	26
Table 3. Density of phantom materials used as density references .....	28
Table 4. Specifications of transducer used for experimental data collection. ....	37
Table 5. Properties of water and skull bone used for calculation of first critical angle of skull bone.....	46
Table 6. Average speed of sound through the calvarium bone layer. Estimated error for the attenuation coefficient values are shown in parenthesis ( $\pm$ ). See Appendix D for error estimation procedure. ....	58
Table 7. Mean and spatial variation of attenuation coefficient values for all fragments studied at 0.5, 1 and 2.25 MHz. Estimated error for the attenuation coefficient values are shown in parenthesis ( $\pm$ ). See Appendix D for error estimation procedure.....	63

## Chapter 1

# Introduction

Ultrasound has proven to be an important medical tool for diagnosis and treatment of several physical disorders. Transcranial ultrasound in particular has become an emergent field of research in recent years. Attention has been drawn to the improvement of existing ultrasound techniques as well as to the development of novel procedures. Transcranial ultrasound presents several opportunities in modern medicine. However, its efficiency is currently far from ideal.

Doppler ultrasound is a popular test that measures the velocity of blood flow through blood vessels. Used in the past for the tracing of blood clots in the principal blood vessels of the legs, it is beginning to be used for transcranial applications. It can help in the diagnosis of cerebral aneurysms and subsequently prevent hemorrhages that can cause severe brain damage or death. This technique is relatively quick and inexpensive, and the equipment used for these tests is becoming increasingly portable (Aaslid et al., 1982; White et al., 2000). The common procedure is to analyze the scattered signal reflected from the internal tissue using a Fast-Fourier transform. However, skull bone can be a highly attenuative medium, decreasing and distorting such reflected ultrasound signals, which poses technical difficulties to both register and interpret them (Ries, 1997).

In recent years, ultrasound contrast agents have been seen as a solution for this problem. Yet, very little is known about how these agents can be used regularly in a clinical environment. Moreover, there is still controversy about the effect of the contrast agents with respect to diagnostic accuracy and it is thought that they may increase the measured flow velocities (Zunker et al., 2002).

Ultrasound aided blood brain barrier disruption is one of the newest techniques in medical ultrasound. The blood-brain barrier is a vascular system that prevents penetration of large molecules as well as almost all small molecules into the brain parenchyma. This barrier unfortunately, also blocks drugs, making very difficult to treat some neural disorders. Microbubble-enhanced-focused ultrasound is currently being investigated for transient and selective disruption of the blood-brain barrier. It has shown promising results in small mammals (Hernot and Klibanov, 2008; Wear 2008), and one group recently reported success in non-human primates (Marquet et al., 2011). The microbubbles are manufactured from biocompatible materials. They are then inserted intravenously and later collapsed by ultrasound irradiation (a phenomenon known as cavitation) at the desired location in the brain. This ultrasound induced cavitation is the principle behind targeted drug delivery and enhancement of drug action (Hernot and Klibanov, 2008).

Blood-brain barrier disruption appears to be a promising technique for drug delivery in the brain. However, ideal parameters and standards are yet to be established. Moreover, attenuative properties of bone present again a challenge for transcranial sonification, especially in humans for which in some cases attenuation can be nearly 100 % at high frequencies.

Now that the understanding of the causes and effects of traumatic brain injury (TBI) has increased, more attention has been drawn to this health problem. Millions of Americans, especially military members actively involved in the recent wars in and around Iraq and Afghanistan, suffer every year from health problems related to TBI. Impacts, sudden acceleration or deceleration of the head, and in particular explosive blasts, are the most common causes of TBI. In fact, recent research indicates that blasts are the most frequent cause of TBI, predominantly mild TBI, among Iraq and Afghanistan combat troops (Centers for Disease Control and Prevention, 2003).

Factors like the chemistry of the explosive, the amount of material detonated, the proximity of the subject to the explosion, the surrounding topography, and the protection used, determine the severity of the lesion (Centers for Disease Control and Prevention, 2003). Some researchers hypothesize that the so-called primary injuries are caused by shock waves propagating through the body, from dense solid and liquid sections to gas-filled organs, such as the lungs, gastrointestinal tract, and middle ear. The resulting physical effects in the brain are difficult to detect directly. However, recent findings suggest that the brain is extremely vulnerable to these primary blast injuries (Ling et al., 2009).

Some medical treatments for blast TBI are beginning to be applied with certain success in the battle field including decompressive craniectomy, cerebral angiography, and transcranial Doppler, among others. Nevertheless, these first trials suggest that the phenomena that cause blast related TBI are much more complex than initially thought. Thus, a more thorough study has to be conducted in order to gain a better understanding of the biomechanics of this problem (Ling et al., 2009). On the

other hand, blast waves are composed of a very wide spectrum of frequencies, and there is no conclusive evidence that a particular range is the cause of TBI.

From previous research, it is easy to conclude that further understanding of the interaction between ultrasound and cranial bone is essential for the success of these medical non-invasive procedures. Furthermore, comprehension of how sound waves are attenuated in the skull is a major area of interest. Such information will be essential to find effective solutions to TBI caused by blast waves.

In the present work ultrasonic properties of bone will be measured at frequencies currently used in medical settings. It is hoped that these results can provide the insight needed to overcome the challenges of transcranial ultrasound and its applications. Moreover, it will be possible to estimate the amount of energy that effectively reaches the brain as a function of frequency. These frequencies are part of the spectrum of blast waves and are, as already stated, relevant for medical purposes in both diagnoses and treatment of neural diseases.

In the next chapters a thorough review of the procedures followed for the data collection, as well as the theory on which they are supported is provided. In chapter 2 basic concepts are given as a guide to understand the procedures followed in the subsequent sections. Later in chapter 3, all the procedures and information concerning the calvarium samples are given. The steps taken to extract the volumetric density of the calvarium specimens from the computed tomographies are detailed in chapter 4. The experimental setups and the procedures followed for ultrasonic data collection are provided in chapter 5. Finally in chapter 6, the results are discussed and compared with those obtained by previous research groups.



## Chapter 2

# Background

Acoustic waves, also known as pressure waves, travel through matter carrying mechanical energy. When these pressure waves vibrate at a frequency above the human hearing range (20 kHz) they are known as ultrasound. The presence of a medium is essential to the transmission of ultrasonic waves, i.e., sound waves cannot propagate in vacuum. The propagation takes the form of a displacement of successive elements of the medium. The elements of material will therefore execute different movements or orbits as the wave passes through them. It is the differences in these movements which characterize basic types of ultrasonic waves (Raj et al., 2004).

### **2.1. Longitudinal Waves**

From all the types of waves, the longitudinal, L wave, or also called compression wave, has been the most widely used since it will travel in liquids, solids, or gases and is easily generated and detected. Longitudinal waves have been used for non-destructive testing (NDT) and materials characterization (Aggelis et al., 2007; Ghoshal, 2008; Lionetto et al., 2005) and longitudinal ultrasound transmission through the human skull is used for imaging, doppler imaging, and therapeutic

purposes (Fry, 1977; Kinoshita et al., 2006; Pichardo et al., 2011). They exist when the motion of the particles in a medium is parallel to the direction of wave propagation, as shown in Figure 1. Alternating compression and rarefaction (low pressure) regions will alternate at the frequency of propagation as the sound travels through the material. Longitudinal waves have a high velocity of propagation in most media compared to other types of waves like shear waves. The wavelengths in common materials are usually very short in comparison with the cross-sectional area of the transducer. This property allows the energy to be focused into a sharp beam with very little lateral distortion. Furthermore, longitudinal waves are easy to convert into shear waves, making them versatile for specific applications (Raj et al., 2004).

## **2.2. Shear Waves**

As shown in Figure 1, shear waves will cause a motion in the material perpendicular to the path of propagation of the wave. Therefore, shear waves can only occur in solid media and highly viscous fluids that can support and propagate shear deformation. Shear can be generated through the process of mode conversion from a pressure wave at oblique incidence to an interface. If the angle of incidence is chosen so that the first critical angle of the material tested is exceeded, then only shear waves propagate into the solid (Schmerr and Song, 2007). In general shear waves are mostly used to characterize the microstructure or to find flaws in a tested material. The speed of propagation of shear waves is proportional to the shear modulus of the material and is usually about half the speed of longitudinal waves.

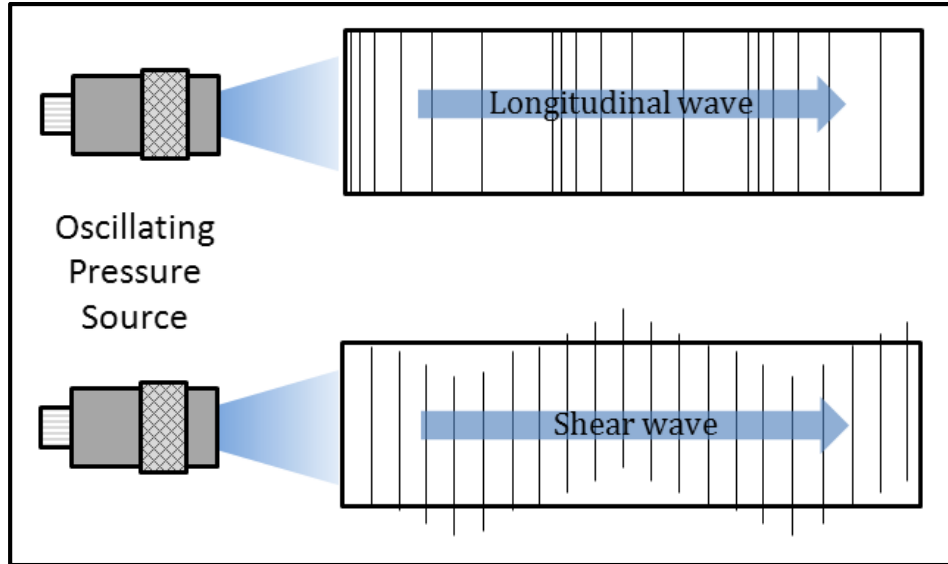


Figure 1. When longitudinal waves propagate through a material, the particles execute an oscillating motion parallel to the direction of propagation. Shear waves will cause a motion in the material perpendicular to the path of propagation of the wave.

### 2.3. Critical Angle

When waves propagate from one material to another, from generalized Snell's law (see Figure 2), the angles of propagation in both materials are related by

$$\frac{\sin(\theta_{p1})}{c_{p1}} = \frac{\sin(\theta_{p2})}{c_{p2}} = \frac{\sin(\theta_{s2})}{c_{s2}}, \quad (2.1)$$

where the sub-indices  $p$  and  $s$  denote longitudinal and shear modes, and sub-indices 1 and 2 denote properties of material 1 and 2 respectively.

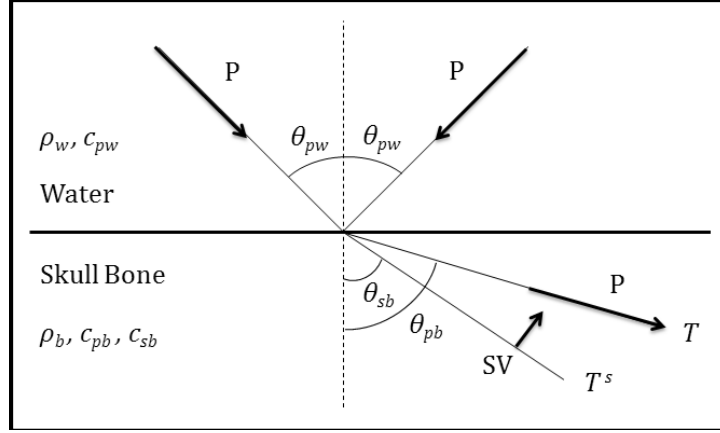


Figure 2. The behavior of incident plane waves at the interface of two media at an oblique angle can be modeled as shown following Snell's generalized law.

Furthermore when the longitudinal waves hit the interface between two different materials at an oblique angle, we have

$$\cos\theta_t = \sqrt{1 - \frac{c_{p1}^2}{c_{p2}^2} \sin^2\theta_i}, \quad (2.2)$$

where  $\theta_i$  is the angle of incidence of the wave at the interface,  $\theta_t$  is the angle of transmission of the wave in the second material, and  $c_{p1}$  and  $c_{p2}$  are the longitudinal wave speeds in materials 1 and 2 respectively.

From this equation it can be seen that when  $\sin\theta_i < c_{p2}/c_{p1}$  the  $\cos\theta_t$  term is real. This condition holds only for the case when the wave speed in the first medium is faster than the speed in the second medium. For the reverse case, the second medium has a faster wave speed, such as in the situation of sound propagating from water to bone. In this case the cosine term will be real for a range of incident angles  $0 \leq \theta \leq \theta_{cr}$ , where the first critical angle  $\theta_{cr}$  can be defined as

$$\theta_{cr} = \sin^{-1}(c_{p1}/c_{p2}). \quad (2.3)$$

As already stated, beyond the first critical angle, only shear waves propagate into the material. In bone, as it will be shown in chapter 5, the first critical angle from the theory will be close to 30 degrees. This theoretical value is in good agreement with the experimental results obtained in (Clement et al., 2004).

Furthermore, there will be a second angle of incidence for which all of the wave energy incident on the interface of the two materials will be reflected or refracted into a surface as shear waves. This angle is known as the second critical angle (Schmerr and Song, 2007; Larson, NDT resource center). This case will not be detailed here since such large angles of incidence will not be encountered in the present study.

## **2.4. Ultrasonic Transducers**

The ultrasonic transducer is the element used to generate and detect ultrasound. By analogy, one can think of a transducer in transmission mode as a stereo speaker and the transducer in reception mode as the human ear. There are different types of transducers depending on the application for which they are designed.

Contact, immersion, and air-coupled transducers are the three most common types of ultrasonic transducers available in the market. The main difference in these three is the coupling media between the face of the transducer and the test sample. As its name indicates, air-coupled transducers use air as the medium for the waves to propagate. They are usually used at low frequencies due to the high impedance mismatch between air and the insonified surface, and for basic applications like

control systems where simple echo detection is needed. Contact transducers, on the contrary, are often used for more refined measurements (NDT, material characterization, etc) and the coupling medium is usually a highly viscous fluid like honey, glycerin, or other lubricant, such that the impedance mismatch between the tested material and the transducer is reduced. In the case of immersion transducers, water is typically used as the coupling medium. The tests are performed with both transducer and sample immersed in a water tank with the distance between them known as the water path (Chen, 2007; Papadakis, 1999; Raj et al., 2004; Ghoshal, 2008).

A schematic of a typical transducer is shown in Figure 3. In general all transducers have the same basic elements: a housing or case for protection of internal components, the circuitry to input and output electrical signals, a piezoelectric element or a composite material that translates the electrical input into vibration and vice versa, an impedance matching material between the vibrating element and the coupling media, and some insulator for noise control (Papadakis, 1999).

The pressure generated from the transducer is transmitted to the coupling medium from most points on the transducer face. Cylindrical transducers are often referred to as piston transducers given that the beam in front of the transducer has a cylinder shaped profile, as shown in Figure 4. The shape and intensity of the beam vary at different distances from the face. Interference and diffraction effects between waves are the cause of fluctuations in intensity at positions close to the source. This section of the beam profile is known as the near field of the transducer. Because of these fluctuations, water paths are usually used outside of this region.

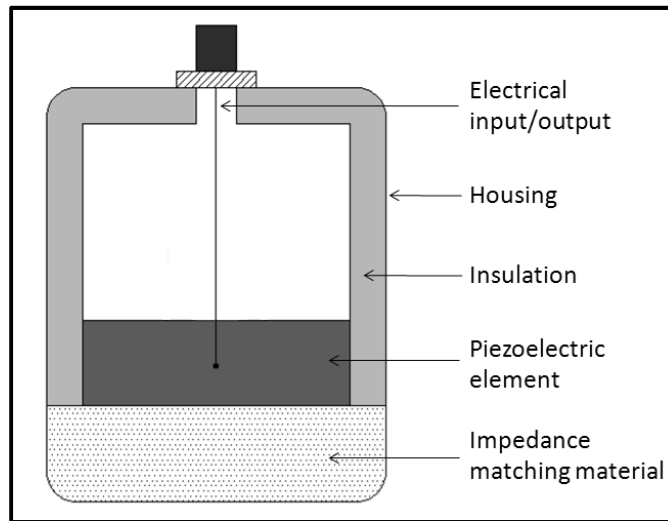


Figure 3. The basic elements of an ultrasound transducer are: housing for protection of internal components, circuitry to input and output electrical signals, piezoelectric element, an impedance matching material, and insulator for noise control.

The region beyond the near field of the ultrasonic beam is known as the far field. Here, the sound beam spreads out in a more uniform fashion. There will be a transition area between near and far field where the beam necks down and the intensity reaches a maximum (for focused transducers). This distance is referred to as the focal length. Optimal detection results are obtained when flaws occur in this area (Larson, NDT resource center). However, in the far field, the beam becomes wider and more uniform (quasi-plane wave) which is ideal for attenuation coefficient measurements.

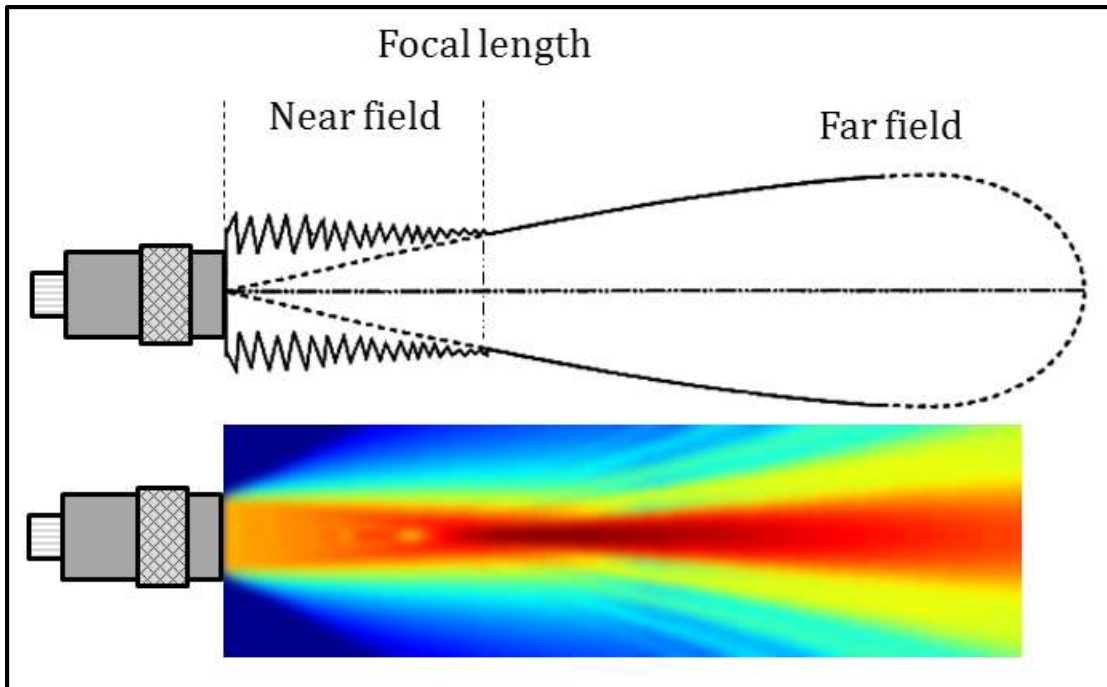


Figure 4. Shape and intensity of the beam vary at different distances from the face. Near field: highly fluctuating intensity region. Far field: sound beam spreads out in a uniform pattern. Focal length: transition area between near and far field where the beam necks down and intensity is higher (Cartz, 1995).

## 2.5. Ultrasound for NDT and Material Characterization

Ultrasound is used for medical evaluations as well as non-destructive industrial inspection. It can be used for imaging for instance in echo-sonography of a fetus in the womb or in the search for cracks in a train wheel. Ultrasound is analogous to other methods of characterization and analysis based on wave-material interaction phenomena (optics, X-ray, infrared, Raman spectroscopy, nuclear magnetic resonance, neutron,  $\gamma$ -ray, mass spectrometry, etc). Ultrasound offers some advantages over other wave-material interaction methods. The main benefits are its portability, cost, applicability to most states of matter, and wide range of properties that can be measured (Chen, 2007).



Different frequency ranges offer solutions to a variety of industrial applications: low ultrasound frequencies (40 kHz – 500 kHz) for sensing and communications; medium–high frequencies (500 kHz-5MHz) are commonly employed for chemical treatment, cleaning, and medical therapy; and high frequencies ( $> 5\text{MHz}$ ) for nondestructive testing in polycrystalline materials such as metals (Aggelis et al., 2007).

In general, the interactions between the ultrasound waves and the tested material are measured and analyzed for NDT and material characterization. Wave speed, attenuation, absorption, and scattering, are the most common properties measured. After propagation of the sound waves through the medium under evaluation, the effect of such interactions on the ultrasound beam can be related to inherent properties of the material.

## **2.6. Measurement Configurations**

Ultrasonic measurements are typically made using two measurement configurations as shown in Figure 5. In a pulse-echo measurement a single transducer is employed as both the source and the receiver. When the incident waves encounter an interface with different impedance (propagating from one medium to another), they reflect due to the acoustic impedance mismatch as shown in Figure 5A. Therefore, in a finite material it is possible to identify, most of the time, two reflections known as the frontwall and the backwall of the material. Reflections that are observed between the frontwall and the backwall correspond to scattering caused

by the microstructure (see scattering chapter 5, section 5.4). This principle governs ultrasound use for microstructure characterization and flaw detection.

The other type of configuration generally used in ultrasonic NDT is the through-transmission configuration. In this case, two transducers are aligned as shown in Figure 5B, one acting as the source and the other as the receiver. Through-transmission is often preferred over pulse-echo for highly attenuative materials given that the waves must propagate only one time through the medium. With this configuration it is possible to measure directly the drop in pressure caused by the material in the path of propagation.

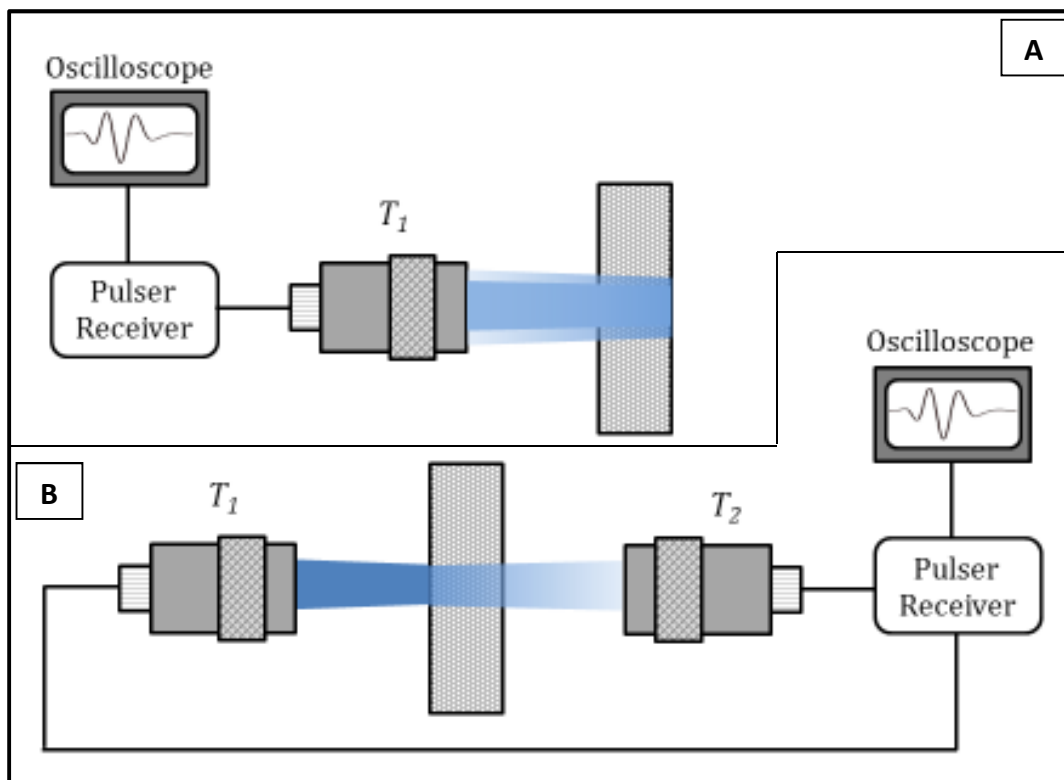


Figure 5. A: In pulse-echo configuration a single transducer is employed as both the source and the receiver. Reflections from the materials in the propagation path are used for evaluation. B: In through transmission, two transducers are aligned, one acting as the source and the other as the receiver. Through-transmission is often preferred over pulse-echo for highly attenuating materials.

These configurations are employed in the present work to assess the geometry of the calvarium samples and the ultrasonic properties of the bone.

## **2.7. A and C Data Acquisition Modes**

The most common mode for ultrasound data collection is the A-mode (A stands for amplitude)(Christopher F. Njeh et al., 1999) . It consists of a time-base display like the one shown at the top of Figure 6. The display shows the amplitude of the signal received by the input transducer as a function of time. In UTWin®, the software employed with the immersion system used in the present work, various parameters such as gain, time-window, sampling rate, and number of averages per second can be adjusted.

The C-scan is a plane composition of multiple A-scans on a surface perpendicular to the incident sound beam. Usually in this mode, the output is a multicolored mesh like the one shown at the bottom of Figure 6. Each color represents the value of either maximum amplitude or time of flight of a preset time gate, shown in yellow in the same figure. However, UTWin® also allows all the waveforms at the locations of the C-scan mesh to be recorded. Furthermore, C-scans can be performed in pulse-echo or through-transmission. These features are exploited in the present work to collect information of the geometry and the ultrasonic properties of the specimens at multiple locations.

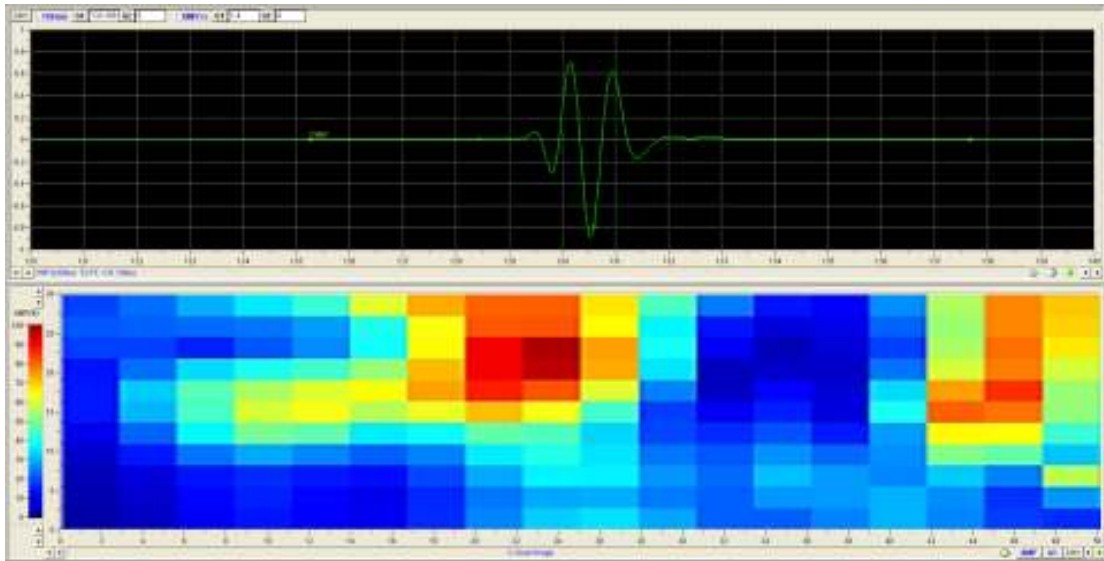


Figure 6. Typical UTWin® display showing both A-mode and C-mode. At the top of the image the received amplitude-modulated signal is presented in a time-base graph. At the bottom, the maximum amplitude at multiple locations of a 2D scan are presented in a multicolored picture.

## Chapter 3

# Calvarium Specimens

The human skeleton, as any other endoskeleton of other vertebrates, is composed of rigid structures called bones. Bones are a type of connective tissue and their main purpose is to provide support to other organs in the body. The hierarchical structural composition of bone plays a major role in its mechanical and ultrasonic properties. For instance, the known compressive strength of bone can be attributed more to the microstructure than to the total bone mass. Furthermore, it has been discussed in various publications that its high ultrasound attenuation is the result of the complexity of its internal microstructure (Aubry et al., 2003; Pichardo et al., 2011).

### **3.1. Human Calvarium**

Since bone is a biological material, it is expected to have a large local variation in its properties. At both the micro and macro-scales the human calvarium and its composing bones exhibit this local variability in properties as well (Smith, 2001). Major changes in curvature, thickness, and density can be encountered in even

small skull areas. This makes the human skull one of the most difficult materials for ultrasound propagation (Aubry et al., 2003).

The human calvarium is composed of the bones that form the calvarium and those that shape the face and the lower jaw or mandible. Specifically the calvarium is formed by eight irregularly shaped bones, as shown in Figure 7: the frontal, two parietal, two temporal, the occipital, and two sphenoids. These bones are held together by means of the sutures. During childhood the sutures are strong, fibrous, elastic tissue that allows the brain to grow and develop inside the head. After full development of the brain, the sutures are no longer flexible and the bones that compose the calvarium fuse and grow together (Rice, 2008).

The bones that compose the calvarium like other bones in the human body have a composed assembly; a sponge-like bone layer known as cancellous bone or diploe, sandwiched between two outer dense structures consisting of cortical bone (Smith, 2001). This composite structure and the complexity of the skull bone microstructure make the calvarium a challenge for ultrasonic transcranial treatment of brain tumors, targeted drug delivery, improved thrombolytic stroke treatment, blood flow imaging, detecting internal bleeding, and tomographic brain imaging (Clement et al., 2004).

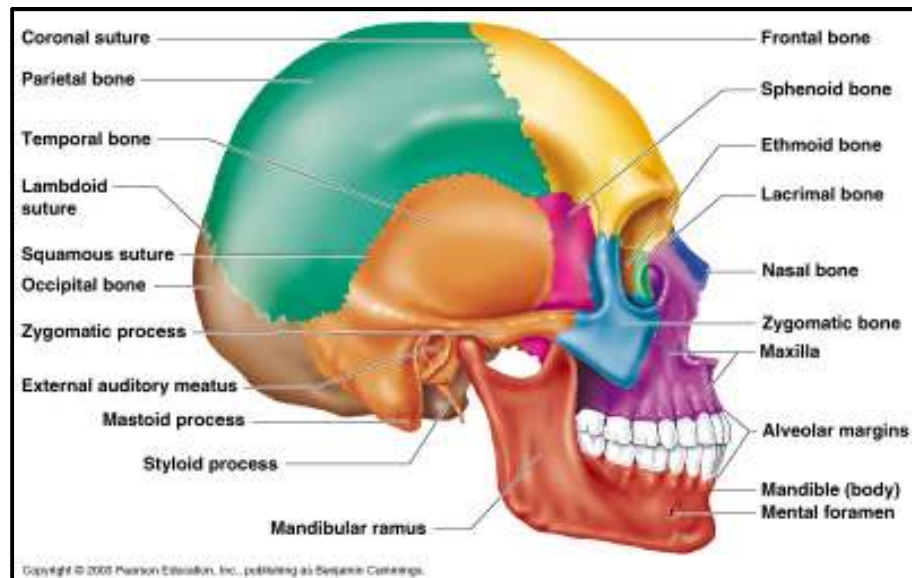


Figure 7. The human skull is composed by several irregularly shaped bones including the lower mandible. The frontal, two parietal, two temporal, the occipital, and the sphenoid bones conform the calvarium.

### 3.2. Excision of Calvarium Specimens

Samples taken from the two laterals, front, posterior, and upper regions of the skull from different donors were used in the present study. It is important to mention that each fragment (depending on the location) may be comprised of material from two or three different bones, including their respective sutures. For instance a specimen excised from the lateral may include temporal, parietal, and sphenoid bone, and the squamous suture. However, multiple bones and sutures in a fragment will be accounted for in the results because properties at each location were recorded.

The samples were excised and kept frozen fresh and sealed at a temperature of  $-20^{\circ}\text{C}$  to prevent degradation. Samples from a total of four donors were taken and the excisions were performed following the regulations and protocols set by the Occupational Safety and Health Administration (OSHA) Standard 1910-1030, “Bloodborne Pathogens”. A Rockwell RK5101K SoniCrafter oscillating saw was

used to perform the excisions. Unlike oscillating saws frequently used in medical settings, this more commercial version has non-sealed moving parts and it is electrically powered. For these reasons it is not recommended for *in vivo* applications. However, it is an ideal tool for the purposes intended in the present work.

Given the irregular geometry of the heads and the variations in size and shape between subjects, the sizes and shapes of the calvarium fragments were not easy to control. Specimens were cut in approximately rectangular pieces with dimensions between 60 mm and 100 mm on each side. A fragment excised from the anterior region of one of the heads is shown in Figure 8. Each fragment was labeled with information about the region of the head from which it was excised, as well as an arrow pointing towards the direction of the face. Information on the age, weight, height, and cause of death of the four calvarium donors are given in Table 1. Donors were labeled from one to four in Roman numerals. Fragments are coded with the number of the head donor followed by a letter (A: anterior, P: posterior, L: left side, R: right side, S: superior) that denotes the region of the calvarium from which it was excised. Thus, for instance a fragment taken from the anterior region of donor I will be referred to as I-A.





Figure 8. Rectangular shaped fragments were excised from frontal, parietal, temporal, and occipital regions of the heads. Samples were kept frozen fresh and sealed to prevent degradation.

Table 1. Relevant information about the calvarium donors.

Donor	Age (years)	Weight (lbs)	Height	Cause of death
I	67	102	6'0"	Lung cancer
II	53	150	5'7"	Cardiomyopathy and kidney disease
III	72	149	5'9"	Prostate cancer and diabetes
IV	60	148	5'10"	Cardiac arrest, ventricular fibulation and HBP

In order to quantify the correlation between ultrasonic properties of calvarium bone with location and density, it was necessary to determine each of these

parameters. Ultrasound echo-pulses and computed tomography images were employed to determine the dimensions and density at every point on the samples. Details of these procedures are given in chapters 4 and 5.

## Chapter 4

# Density from Computed Tomography

The principle behind computed tomography (CT) was proposed prior to the development of the first automated processors. Perhaps the first fully functional CT scanner used for medical applications was designed by Godfrey N. Hounsfield in 1967. Currently CT is one of the most popular techniques for biomedical non-invasive evaluation. The image reconstruction that takes place in a CT scanner, and that was first enunciated in the 1940's, follows the idea that by evaluating 2D projections of an object from multiple angles, the internal composition of such 3D object can be regenerated. As shown in Figure 9, imagine that a 3D image of the round objects behind the blocks is intended. When seen from different angles, and if all objects are translucent to the eye, it will be eventually possible to determine the fact that there are three oblong objects behind the blue blocks. In computed tomographers, these 2D projections are regular X-ray images and literally dozens and sometimes hundreds of these X-rays are collected in modern scanners for 3D reconstruction (Hsieh, 2003).

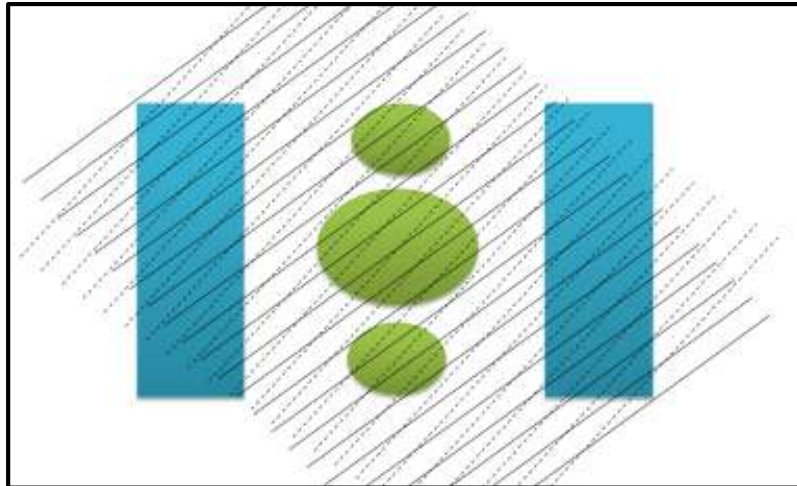


Figure 9. A 3D CT image is reconstructed from several 2D x-rays. These 2D x-rays are taken at slightly different angles around the 360 degrees. Then, a code following a simple algorithm first proposed in the 1940's, makes sense of all the different projections and composes the 3D image.

#### 4.1. Computed Tomography in Biomaterials

In biomaterials, internal structure reconstruction is possible because of the penetration of X-rays in the tissue. Thus, through-transmission X-ray measurements are performed and the material attenuation is measured. The amount that the X-ray beam is attenuated characterizes the material that lies in the propagation path. The variation in intensity (attenuation coefficient) used in current tomographers is measured in Hounsfield units. Hounsfield units are relative units that compare the attenuation coefficient of a medium with that of water (Feeman, 2010).

The recent development of quantitative computed tomography (QCT) has allowed for bone mineral density (BMD) measurements to be made. The measurements have been widely performed in the axial spine and peripheral skeleton to determine in three dimensions the volumetric density of trabecular and cortical bone. QCT has also been used to estimate fracture risk, age-related bone loss, and as a

non-invasive evaluation tool for chronic and metabolic diseases, like osteoporosis (Brunader and Shelton, 2002).

CT and QCT are beginning to receive more attention among researchers in the field of acoustics. CT and QCT are attractive given that they can provide with information on the density as well as the microarchitecture of bone, which allows for a more accurate modeling of the acoustic properties (Aubry et al., 2003).

Further advances have been made in the field of computed tomography. Volumetric QCT (vQCT) has been explored recently for medical applications. It can provide a more direct relationship between the microstructure of bone and its mechanical properties (Laugier et al., 1993). High-resolution peripheral quantitative computed tomography (HR-pQCT) makes it possible to evaluate the microstructure of bone in the distal radius and tibia (Sekhon et al., 2009).

For QCT, the use of reference phantoms for calibration of the CT images is a common practice. These phantom materials are materials for which the density is known by some other independent measurements. Then, X-ray intensity values (Hounsfield units) can be converted into actual bone density. Furthermore, the reference phantom helps to correct for errors caused by artifacts or poor resolution (Brunader and Shelton, 2002). Three polymers with known density were used in the present study for calibration purposes.

#### **4.2. Phantom Materials**

Measurement of bone density presents practical difficulties. Bone in the calvarium is composed of cortical bone, cancellous bone, and pores filled with bone

marrow. All three components appear in different proportion at every location of the skeleton. Furthermore, these three components have different densities. Thus, as any other biometric, bone density has been determined as a statistical approximation of densities from large sections, or from bone ashes (in an attempt to measure the density of bone mineral alone). As already stated, CT imaging has been used for quantitative bone densitometry. Scans are performed with reference materials and real density is then extracted from the CT images.

In the present work, mean values of skull bone density from previous works (see Table 2) were considered in the selection of the reference materials. Three polymers with standard densities similar to the mean densities of cortical bone, cancellous bone, and bone marrow, were selected as phantoms. Polymers have the advantage of being very homogeneous, i.e., their properties do not vary significantly with location. Therefore, the measured densities represent the density at every point in the reference, which is desirable in order for the density results to be corrected at every slice of the CT scans. Finally, after evaluation of these factors, polytetrafluoroethylene, polycarbonate, and low density polyethylene were selected as phantom materials.

Table 2. Density of bone mineral and compact bone ashing previously reported (Rustgi et al., 1980).

	<b>Bone Mineral Density (g/cm<sup>3</sup>)</b>	<b>Compact Bone Density (g/cm<sup>3</sup>)</b>
Mean	1.346 ± 0.067	2.140 ± 0.085

In order to determine the density of the reference materials, a Toledo Mettler AT201 Electronic Analytical SemiMicro Balance, shown in Figure 10, was employed.

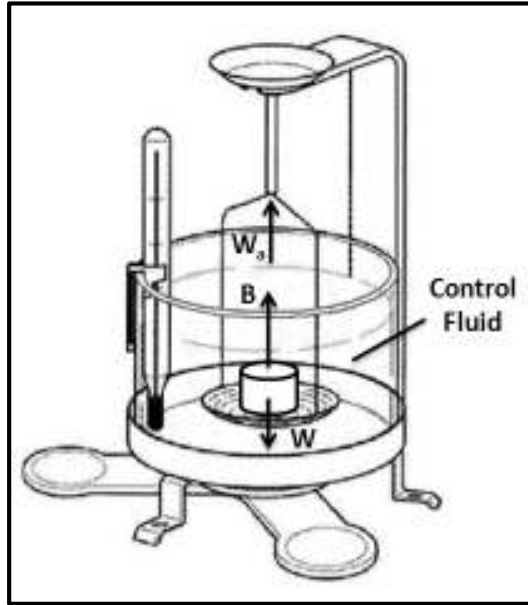


Figure 10. Density measurements were performed with a Toledo Mettler AT201 electronic analytical semimicro balance. Making use of a reference fluid for which the density is known, the Archimedes buoyance principle was applied.

Following the Archimedes principle, when an object is immersed in a fluid, the fluid applies a force to the object equivalent in magnitude to the weight of the volume displaced and in opposite direction to the acceleration of gravity. Assuming that the object is in equilibrium, the net force is zero so that

$$W_a + B - W = 0, \quad (4.1)$$

where  $W_a$  is the tension in the holder (the apparent weight of the object) and  $W$  is the weight of the object. The buoyant force  $B$  is given by

$$B = \rho_{fluid} V g, \quad (4.2)$$

where  $V$  is the volume of the object,  $\rho_{fluid}$  is the density of the fluid, and  $g$  is the acceleration of gravity. Combining these two equations it can be shown that

$$\rho = \frac{M}{M - M_a} \rho_{fluid}, \quad (4.3)$$

where  $M$  is the total mass of the object (determined from the weight in air,  $M = W/g$ ), and  $M_a$  is the apparent mass (determined from the weight in the fluid,  $M_a = W_a/g$ ). Note that further simplification can be made so that the masses can be replaced by the weights directly measured with the instrument.

Water was the fluid used to measure the density of polytetrafluoroethylene and polycarbonate, because both are denser than water. In the case of low density polyethylene, which is less dense than water, it was necessary to utilize ethanol. The results of these measurements are given in Table 3.

Table 3. Density of phantom materials used as density references

Material	Density (g/cm <sup>3</sup> )
Polytetrafluoroethylene	2.16
Polycarbonate	1.19
Low density polyethylene	0.93

#### 4.3. Conversion of Hounsfield Units to Real Density

All studied samples were scanned using a Light Speed Plus 16-Slice CT scanner at the BryanLGH Medical Center-West, Radiologic Services, Lincoln,



Nebraska. A picture of the actual CT scanner employed for the density data collection is shown in Figure 11. The three phantoms were scanned along with the bone samples every time. Scanning the references with the samples every time prevents errors due to variations in calibration and test conditions.



Figure 11. Calvarium specimens were CT scanned using a Light Speed Plus 16-Slice CT scanner at the BryanLGH Medical Center-West, Radiologic Services, Lincoln, Nebraska.

The images (in DICOM format) were analyzed with the CT image processing and editing software Mimics®. The Digital Imaging and Communications in Medicine (DICOM) standard was created by the American College of Radiology (ACR) and the National Electrical Manufacturers Association (NEMA) to standardize medical images, such as CT scans, MRIs, and ultrasound (Digital imaging and communications in medicine (DICOM) part 10: Media storage and file format for media interchange 2007).

When the sets of these DICOM files are imported into Mimics®, the software reconstructs the independent slices into a 3D model. The images are depicted in a grey scale in Hounsfield units. Making use of the tool for density determination,

densities of the phantom areas of the images at different depths were determined, as shown in Figure 12. Correlation curves were constructed with these data for each CT session. These correlation curves are presented in Figure 13.

Even though commercial codes like Mimics® allow for density measurements on adjustable areas of the image, this procedure has to be done on individual locations one at a time and on each 2D slice. Thus, in order to determine the volumetric density at multiple locations on the fragments in a more efficient manner, it was necessary to manipulate the raw data from the DICOM files. Consequently, it was essential to understand first the nature of these images and how they are preprocessed and reconstructed.

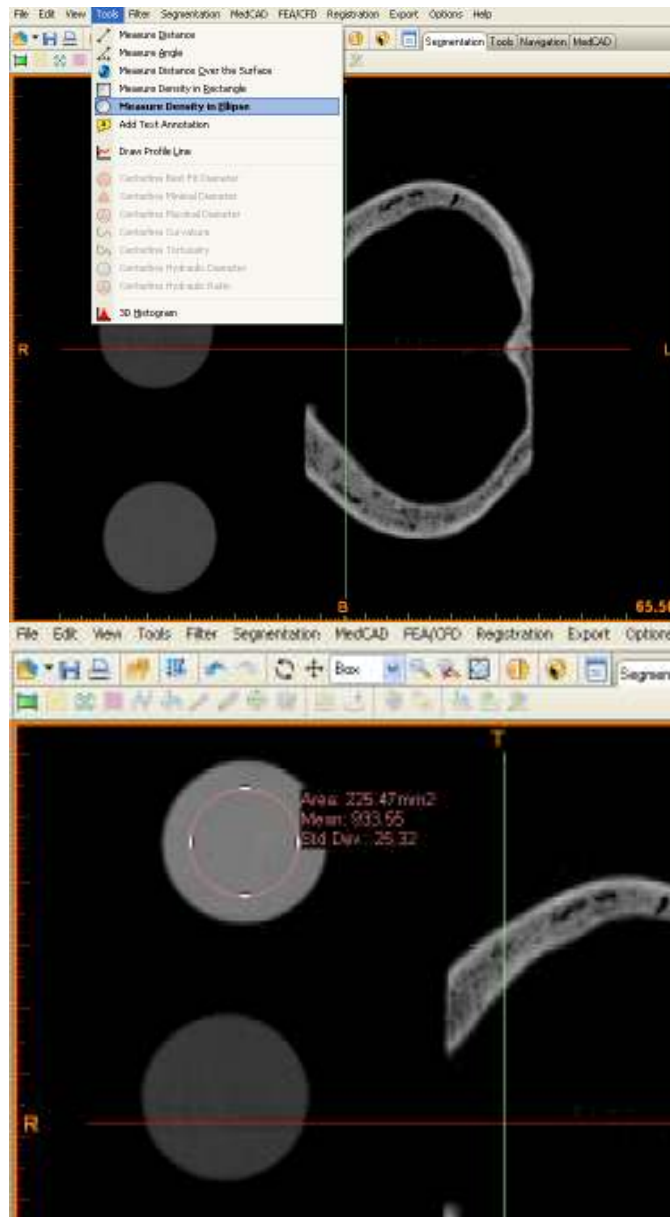


Figure 12. With the tool for density determination, densities on the phantom areas of the images at different depths were determined. A correlation curve was constructed with these data for each CT session.

A single DICOM file contains file meta-information header and an image information object. The file meta-information header is composed of a 128-byte file preamble, a 4-byte DICOM prefix, and the file meta-elements. DICOM image data can be compressed (encapsulated) to reduce the image size. Files are often

compressed using lossy or lossless variants of the JPEG format, and sometimes private information about the patient is encoded within the files (Bankman, 2003).

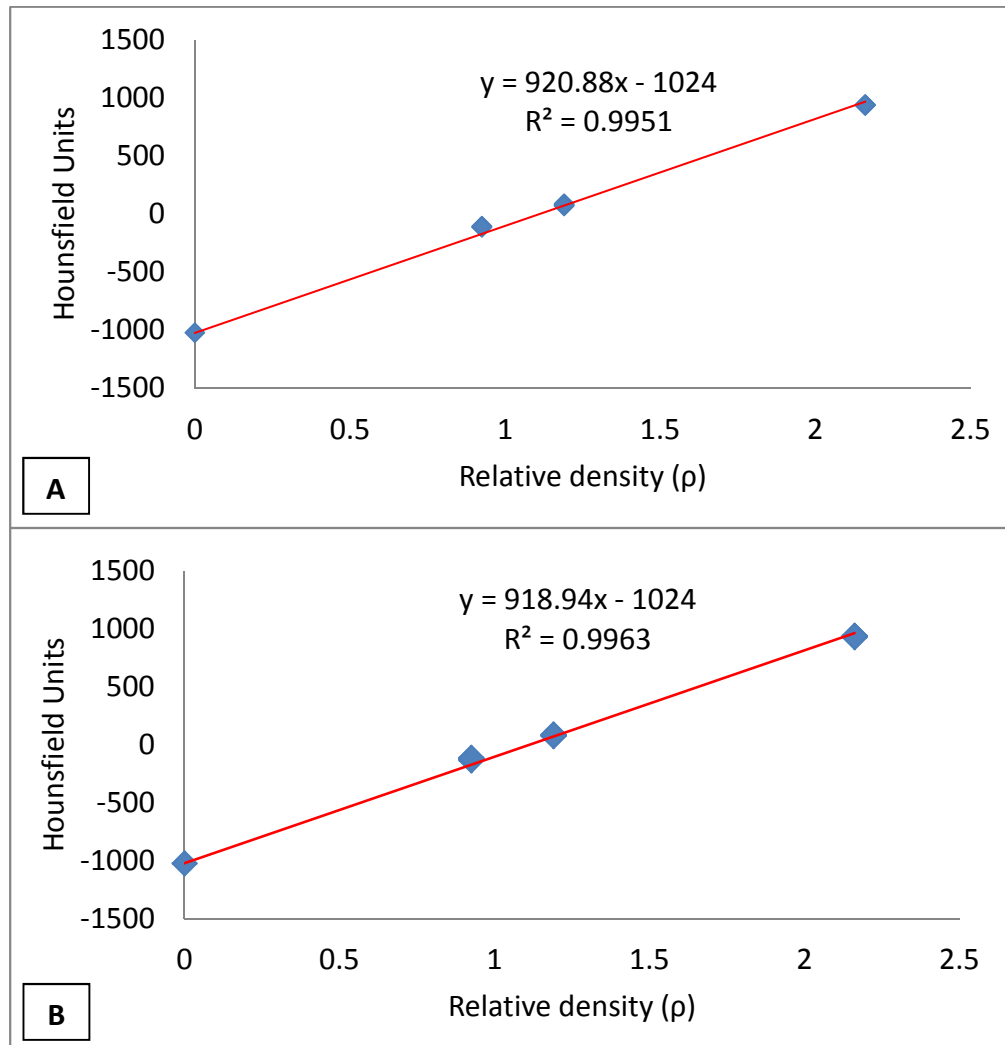


Figure 13. Correlation curves were determined for each session from pixel data in Hounsfield units of the reference materials in the CT images and their respective measured density. A: correlation curve for first CT scanning session. B: correlation curve for second CT scanning session

Another transformation that is commonly performed on the images is the pixel padding correction. Pixel padding is generally intended to convert circular images (most CT images are circular) into rectangular images for better presentation. Pixel padding values are always out of the range of possible values in the image, (usually

large negative numbers) which make them easy to identify. In commercial DICOM images analysis software, these padding pixels are reassigned a value that corresponds to that of air. As it can be seen in Figure 14, the original circular CT image has been transformed in Mimics® into a rectangular image. The pixels corresponding to the padded area out of the circle have been assigned the same grey scale value of air so they appear black on the image.

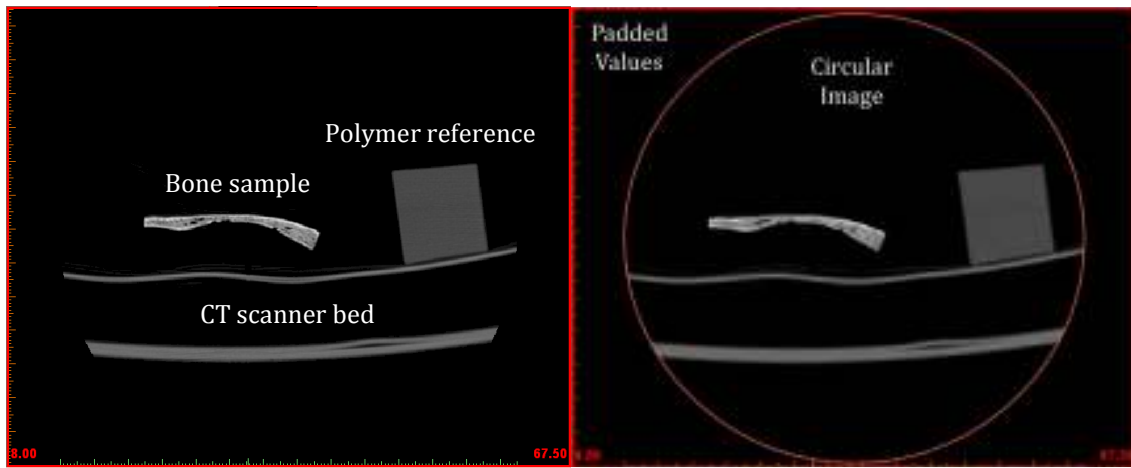


Figure 14. The CT images used in the present work were circular images padded with values of -2000 before slope and intercept correction. Padded values in Mimics® are assigned a value of zero before correction for which they appear black (air) on the image.

Finally, from the values of rescale slope and rescale intercept, included in the header by the manufacturer, the pixel values are corrected and converted to Hounsfield units. This correction is performed assuming a linear relation

$$\text{Hounsfield Units} = pv * m + b, \quad (4.4)$$

where  $m$  is the rescale slope,  $b$  is the rescale intercept, and  $pv$  is the pixel value from DICOM pixel raw data.

Following the aforementioned corrections, the steps to convert raw DICOM files to density were as follows:

1. Pixels with the padding value (-2000) were reassigned air values (0)
2. Rescale slope and rescale intercept values were extracted from the file header.
3. Pixel values were rescaled to Hounsfield units.

This data conversion was done using a Matlab code that follows the logic presented in Figure 15. The Matlab code is provided in Appendix A.

#### **4.4. Mean volumetric Density Determination**

In order to correlate density and the measured ultrasonic properties of skull bone, mean density values were calculated on areas with a size that matches the step size in the C-scans performed for determination of wave speed and attenuation coefficient. A code in Matlab® was written to identify those areas within the skull fragment based on the Hounsfield units corresponding to all pixels in the sub-matrix. Later, mean values on each area were averaged throughout a normal projection across the bone thickness, giving as a result, a matrix of volumetric mean density values at the same locations where ultrasonic properties were determined. In Figure 15 a schematic of the approach followed in the algorithm is shown for determining the mean volumetric density at different locations on the fragments. Note that following the same idea thickness and curvature at the same locations can be determined. In Figure 16 the results of the mean volumetric density matrix for fragment IV-A are shown. In the present work ultrasound pulse-echoes were used also to determine thickness and angle of incidence.

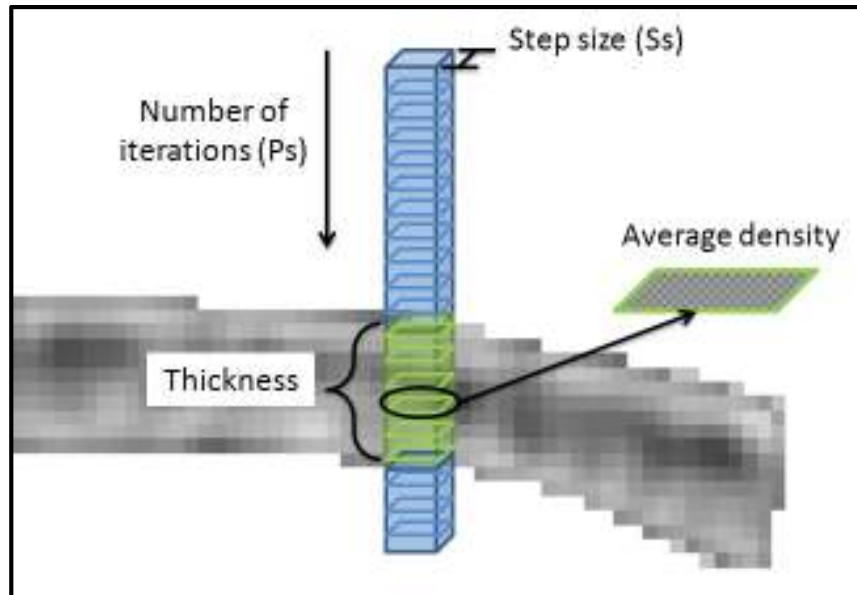


Figure 15. Ps: pixel size. Ss: step size. Mean density values were volumetrically determined from CT images. An algorithm written in Matlab® would identify the areas within the skull fragments based on the Hounsfield units of each pixel. Mean density values on each area were averaged in normal projection across the specimen thickness.

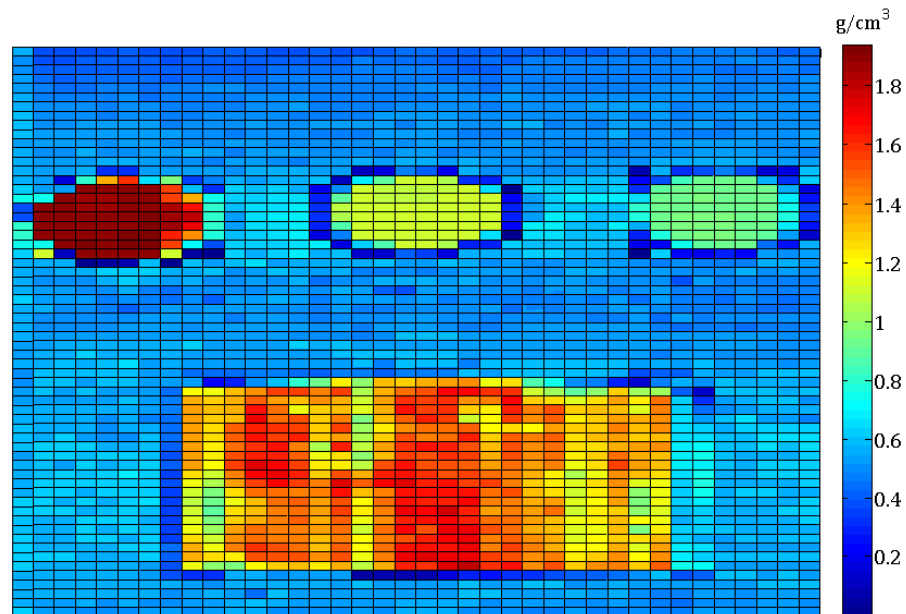


Figure 16. Volumetric average densities were determined at various locations on the CT images. From this matrix the densities of a region corresponding to that where the ultrasonic properties were measured, was later extracted.

## Chapter 5

# Propagation of Ultrasound through Human Calvarium

In this chapter all aspects of ultrasound data collection are presented.

Ultrasonic techniques are employed to measure geometric properties of the calvarium bone specimens. Later, geometric data combined with densities extracted from CT files are used for determination of energy loss and attenuation coefficients. In the following sections of chapter 5, a brief summary of the equipment used in the experimental setup is provided. Then, the steps taken to collect the ultrasonic data are detailed. First a description is given about how the geometry of the specimens was assessed by the means of pulse-echo configuration. Then the procedure to determine total energy loss and attenuation coefficients from through-transmission data is described.

### 5.1. Equipment

#### Transducers





Four ultrasound transducers with central frequencies of 0.5, 1, 2.25, and 5 MHz, respectively, were used in the present investigation. These frequencies are



found in the frequency profile of blast waves and are also relevant for medical purposes in both diagnoses and treatment of neural diseases. The transducer manufacturer specifications are presented in the Table 4.

Note that the V (videoscan) Olympus Panametrics series is designed to provide heavily damped broadband performance. They are, as suggested by the manufacturer, the best choice in applications where there is high attenuation or scattering (Olympus. Inspection and Measurement Systems).

Table 4. Specifications of transducer used for experimental data collection.

Image	Frequency	Case Size	Series	Focal Depth
	0.5 MHz	0.75"	Olympus Panametrics V318-SU	Unfocused
	1 MHz	1"	Olympus Panametrics V302-SU	4"
	2.25 MHz	0.5"	NDT Automation IU2G2	3"
	5 MHz	0.5"	Olympus Panametrics V309-SU	Unfocused

### **Sound Absorbing Foam**

When the sound beam propagates through the water in the test tank, it hits the target (calvarium fragment) and scatters in different directions (see scattering in chapter 5, section 5.4). These scattered waves can then reflect on other objects in the tank and the walls of the tank itself. Part of these reflections may be received by the transducer creating a noisy signal. To prevent this artifact it is often recommended to pad the tank internally with sound absorbers. In this work it was decided to place a dividing wall between the sample and the source transducer. The absorber prevents noise from reflections on the sample holder and tank walls. Different commercial sound absorbing foams were evaluated. The desired properties were adequate sound-absorbing properties, water degradation resistance, and good performance after complete immersion in water. Acoustical Polypropylene Foam Absorber, .40 NRC, was found to have all desired properties. This foam is made of small foam beads clustered together in one block. These non-connected beads provide porosity to the foam but prevent water from permeating into it. Thus, the sound absorbing properties (nominal 40% noise reduction) are preserved and the foam does not degrade.

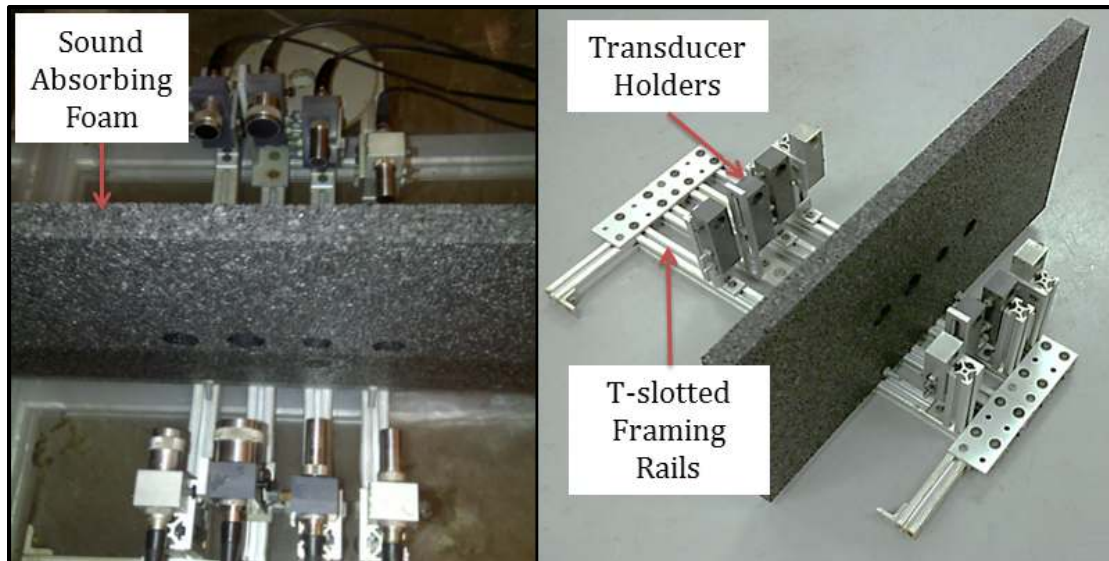


Figure 17. Multi-transducer fixture made with t-slotted framing allowed the placement of transducer holders and sound absorbing foam wall. The distance between transducers can be adjusted.

### Multi-transducer holder

In order to place transducer pairs in good alignment for through-transmission measurements, a multi-transducer holder was designed and built. A simple design constructed with t-slotted framing offered great versatility. T-slotted framing can be easily assembled, it is made in corrosion resistant aluminum, and a variety of available prefabricated accessories make the fixture inexpensive and easy to modify. The fixture shown in Figure 17 consists of four rails along which the distance between transducer pairs can be adjusted. The eight holders allow the transducers to be quickly attached and replaced. Finally the sound absorbing foam wall was fixed to the fixture by the means of 90° single-hole brackets.

## 5.2. Experimental Procedure

The experimental setup and equipment used in the present work for the determination of ultrasonic properties of human calvarium are shown in Figure 18.

Ultrasound measurements were performed in a Mistras immersion system designed for standard ultrasonic transducer characterization and testing. The system is integrated with a water tank and an automated motion system. The system can be moved manually or automatically. Automatic motion is provided by a stepper motor power supply and driver. Besides the motion, every parameter of a test can be modified from the software interface UTWin E 2.00. Wave forms are generated by a built-in function generator (Agilent 33250A). Data can be recorded and analyzed with a built-in oscilloscope, Tektronix TD3032 Interface board SMC-4-PCI, UT Bridge System 1600-8000, and Digital Multimeter DVM Fluke 179 with AD-1210-PCI (12 Bit Analog to Digital Converter Board).

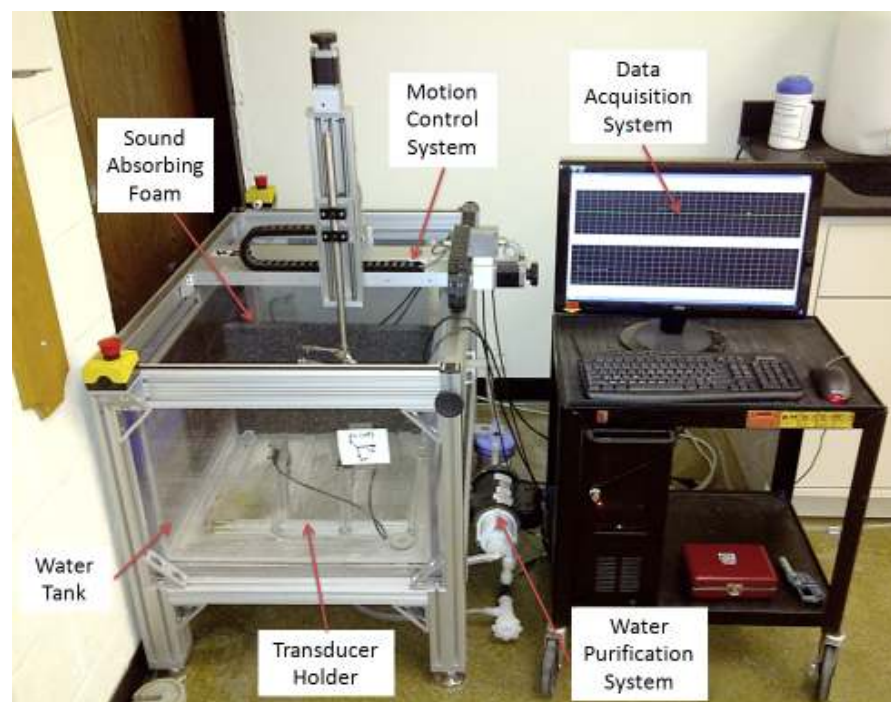
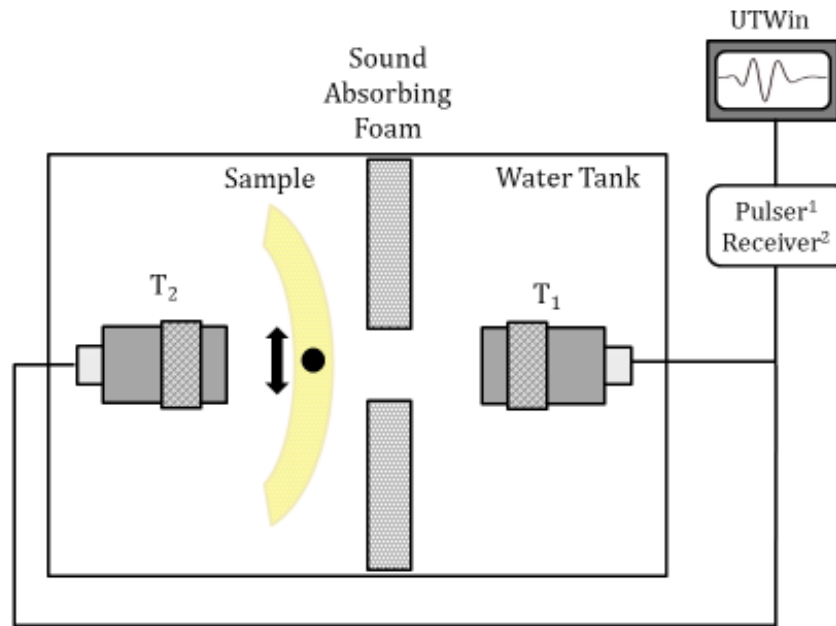


Figure 18. Ultrasound evaluation was performed in a Mistras immersion system: Motion control system, water purification system, immersion water tank, data acquisition system controlled with UTWin software. Transducers were placed in a trough-transmission set up with the aid of the multi-transducer fixture.

The surface of the specimens was scanned making use of the automated motion control system. Parameters such as step size and scanning speed can be

tailored to the study. Both parameters were defined taking into account the size of the ultrasound beam of the four transducers used and the total area of the samples. The temperature of water in the tank was monitored during the experiments. Temperature data are needed to determine the sound speed in water.

Through-transmission and pulse-echo signals were recorded at each location of the C-scan mesh. Transducers were placed in the custom made multi-transducer holder and checked for good alignment between transducer pairs. Alignment was ensured first by adjusting carefully the transducer holders and then by looking at the reference transmitted pulse in through-transmission configuration. The transducers were moved back and forth and the highest amplitude in the transmitted pulse when moving the transducer was an indication of the location of good alignment.

### **5.3. Ultrasound for Thickness and Curvature Measurements**

Ultrasonic techniques were used to estimate the thickness and curvature of the specimens. Pulse-echo signals were recorded and used for both calculations.

#### **Thickness Measurement**

The thickness at the same points at which the through-transmissions were performed was determined using a cross-correlation function. The reference consisted of a perfectly flat target for which the thickness  $t$  was known.

In Figure 19 the approach followed to determine the thickness is shown schematically. Pulses collected from a C-scan performed from both sides of the sample were cross-correlated with those from the reference.

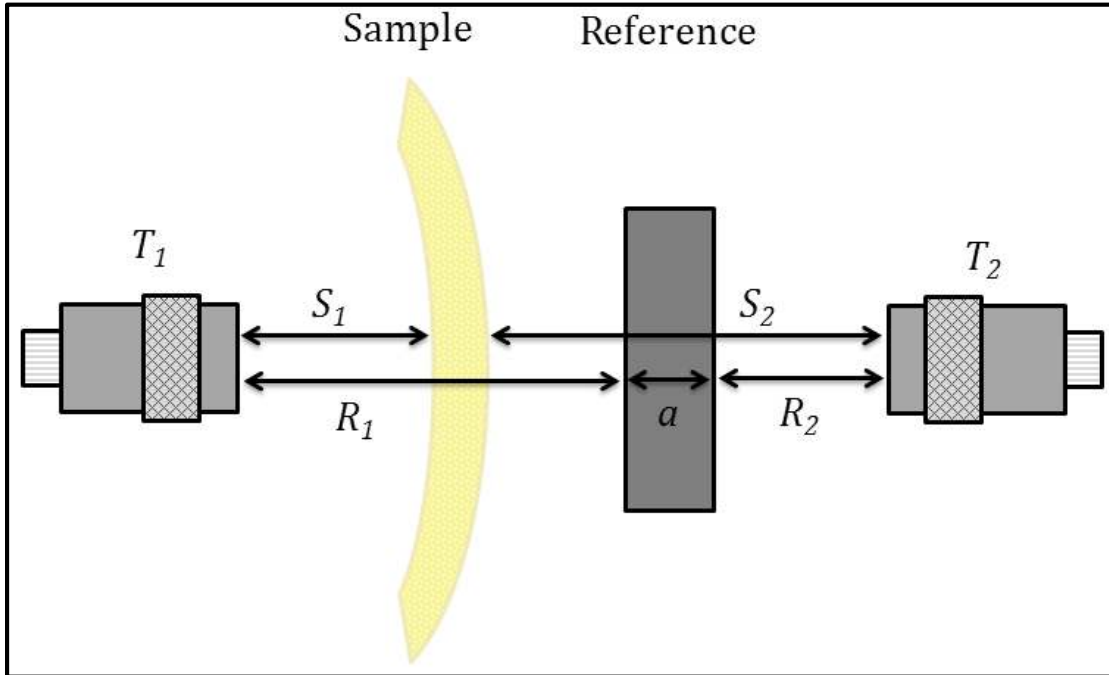


Figure 19. Thickness at different locations on the specimens were determined using a cross-correlation function between reference echo pulses from a perfectly flat target and echo pulses from both sides of the fragment.

For the thickness calculation

$$D = R_1 - S_1 + a + R_2 - S_2 , \quad (5.1)$$

where  $R_i$  is the distance from the transducer face to the reference and  $S_i$  is the distance from the face of the transducer to the calvarium fragment from sides 1 and 2 respectively.

From the Eq. (5.1) one can see that  $R_1 - S_1$  and  $R_2 - S_2$  correspond to the spatial difference between the pulses from the sample and the reference. Such differences were determined by cross-correlating the signals. Finally, the thickness is given by

$$D = a + (t_{cc1} - t_{cc2}) \frac{c_w}{2} , \quad (5.2)$$

where  $c_w$  is the speed of sound in water at the measured temperature and  $t_{cc}$  is the cross-correlation time delay from each side of the fragment. The signals from each side of both the reference and one location of a calvarium fragment are depicted in Figure 20.

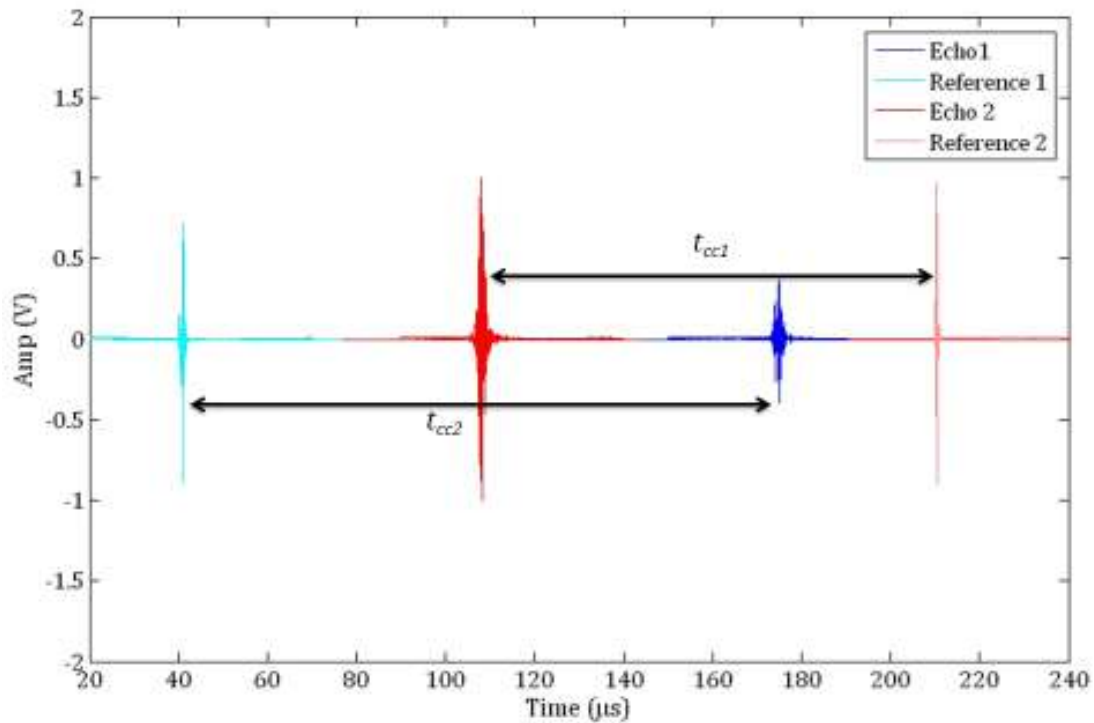


Figure 20. Values  $t_{cc1}$  and  $t_{cc2}$  are the time of flight differences between reference and specimen echo pulses. Echo1: reflection from the concave side of the specimen, Echo2: reflection from the convex side of the specimen, Reference 1: reflection from side 1 of flat target, Reference 2: reflection from side 2 of flat target.

### Angle of Incidence

The behavior of incident plane waves at the interface of two media at an oblique angle differs from the same phenomena at normal incidence. At very shallow angles part of the longitudinal incident L-wave energy will propagate through the material in shear mode. Because the calvaria fragments are curved, there will be



many locations in the C-scan mesh for which the angle of incidence was not normal. It is then necessary to quantify those angles of incidence and to understand the effect of such angles on the transmission.

The change in transmission coefficient as a function of the angle of incidence can be expressed as (Schmerr and Song, 2007),

$$T = \frac{2\cos(\theta_{pw})[1-2\sin^2(\theta_{sb})]}{\cos(\theta_{pb}) + \frac{\rho_b c_{pb}}{\rho_w c_{pw}} \cos(\theta_{pw})\Delta}, \quad (5.3)$$

where

$$\Delta = \left(\frac{c_{sb}}{c_{pb}}\right)^2 \sin(\theta_{sb}) \cos(\theta_{sb}) \sin(\theta_{pb}) \cos(\theta_{pb}) + 1 - 4(\sin(\theta_{sb}) \cos(\theta_{sb}))^2. \quad (5.4)$$

Transmission coefficient as a function of angle of incidence is shown in Figure 21 using properties of a bone water interface. It can be seen that transmission is small at normal incidence and remains almost constant until incidence at nearly the first critical angle. Furthermore, note that from the Eq. (2.3) it can be shown that at angles of incidence below the critical angle, the transmission coefficient will be a real number independent of the frequency. Moreover, it has been demonstrated that below the first critical angle a transmitted wave pulse will have different amplitude from the incident wave but will have exactly the same shape as that of the incident wave (Schmerr and Song, 2007). In conclusion, at angles of incidence safely below the first critical angle, normal incidence can be assumed without incurring large errors from transmission or pulse distortion.

In order to estimate the angles of incidence in the calvarium fragments the same data used for thickness calculation were utilized. The surface profile was

reconstructed using the echo data on the convex side of the fragment. This initial surface was smoothed by fitting a polynomial surface to it. Finally, the surface gradients, and subsequently the angle of incidence, were computed at the same locations where the properties were measured. The angles of incidence at various locations of fragment I-S are shown in Figure 22 as an example.

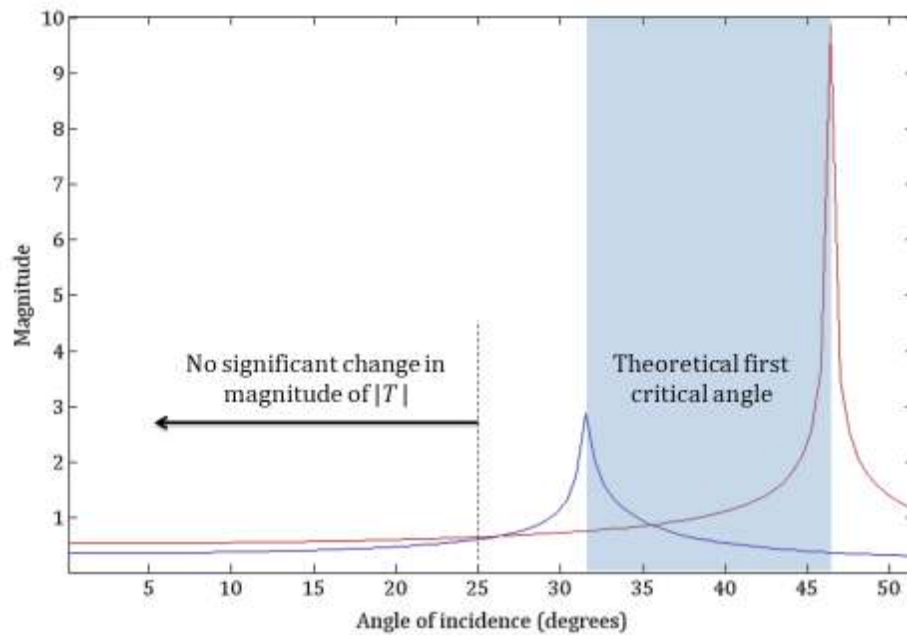


Figure 21. Transmission coefficient is small at normal incidence and remains almost constant until incidence at nearly the first critical angle. Experimental values of shear and longitudinal wave speed through bone and water, and densities for bone and water taken from the literature are shown in Table 5.

Table 5. Properties of water and skull bone used for calculation of first critical angle of skull bone.

	Cp (m/s)	Cs (m/s)	Density (g/cm <sup>3</sup> )
<b>Water</b>	1467		1
<b>Skull bone</b>	2053-2504	1360-1640	2-2.4

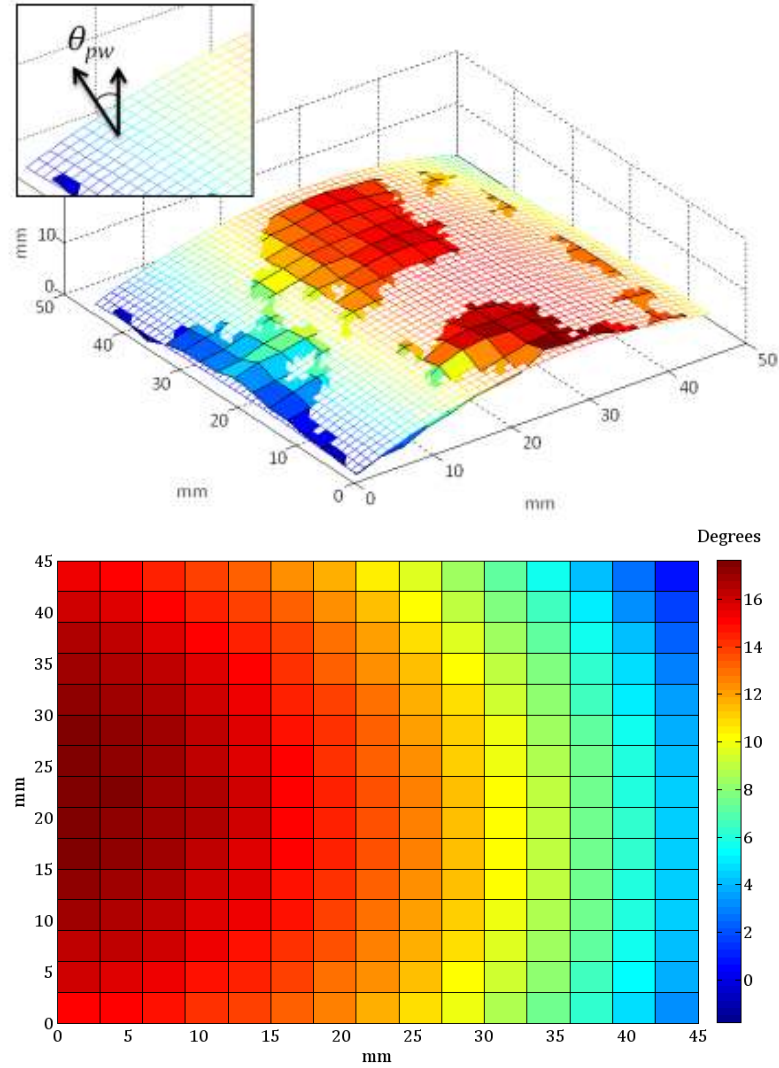


Figure 22. Surface profile of fragment I-S was reconstructed using the echo data on the convex side of the fragment. A polynomial surface was fit and the surface gradients were computed at the same locations where ultrasound properties were measured.

#### 5.4. Measurement of ultrasound properties

##### Wave speed

The calculation of the ultrasonic energy propagation speed through a given material is a useful tool for the determination of mechanical and ultrasonic properties as well as information about the condition and dimensions of an element.

There are a number of different types of speeds or velocities that can be discussed. The most significant are referred to as phase velocity, group velocity, and signal velocity (generally equal to group velocity under conditions of normal dispersion). Each of these terms covers a complex phenomenon and they should not be confused with each other. Group speed is a term used to indicate the speed with which the energy is propagated when the wave is amplitude-modulated. It is the speed of propagation of a set of harmonic waves and this is the speed referred to when the terms wave speed or wave velocity are loosely used (Chen, 2007). The group speed is usually the most frequently measured in solid materials, including bone. However, sometimes assessing phase speed is desirable for a direct measurement of dispersion (frequency dependence of phase speed) (Azhari, 2010; Fry and Barger, 1978).

Here, the wave speed in skull is measured relative to the wave speed in water. The method followed is that already used in many previous works (Bauer et al 2008, Wear 2000, White et al. 2006, Pichardo et al 2010). Cross-correlation is done using signals from measurements performed with and without the calvarium fragment. The wave speed can be expressed as

$$c_b = \frac{D}{\frac{D}{c_w} - |t_{cc}|}, \quad (5.5)$$

where  $c_b$  is the speed of sound in bone,  $D$  is the thickness of the fragment at the tested location,  $c_w$  is the speed of sound in water at the measured temperature, and  $t_{cc}$  is the cross-correlation time delay. This time delay and the subsequent alignment through a cross-correlation function between the signals are shown in Figure 23-A and Figure 23-B respectively.

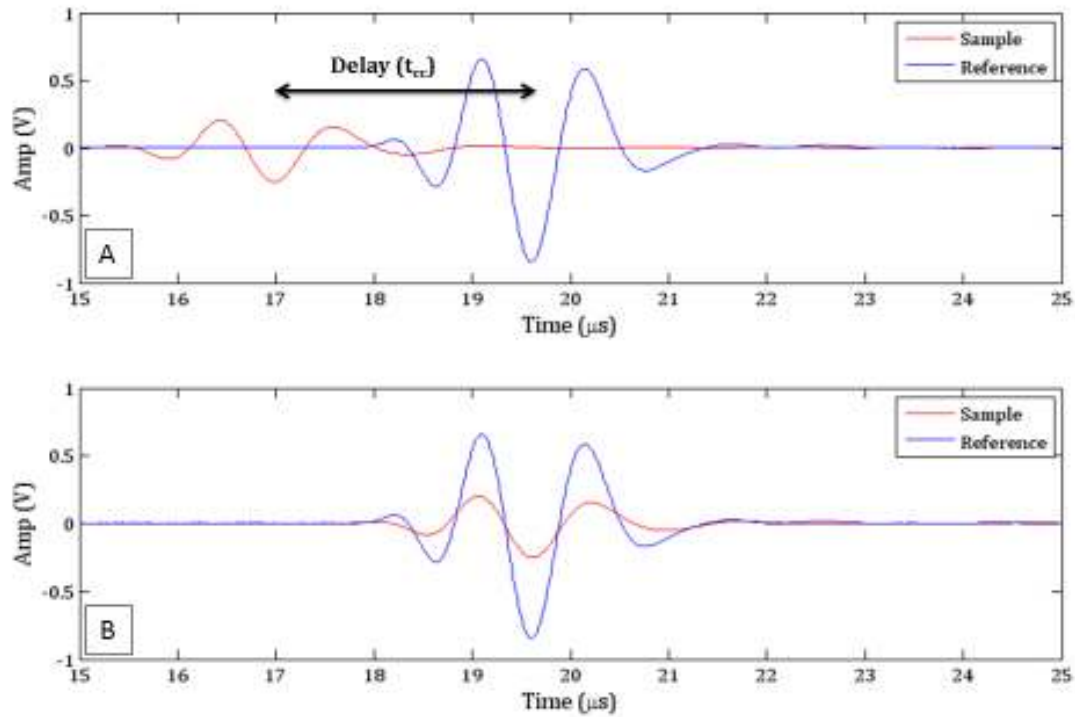


Figure 23. A: Reference waveform is delayed with respect to sample waveform. The delay is the result of a higher speed of propagation of sound in the skull bone than in water. B: When both pulses are in perfect alignment, the cross-correlation function reaches a maximum value. From this time delay  $t_{cc}$  can be determined.

### Attenuation, scattering, and absorption

Attenuation, scattering, and absorption are usually concepts that can be confused and often misused when talking about the energy loss caused by a material on the ultrasonic beam. When a pressure wave travels through a real material, the energy is diminished by two phenomena: one portion of the energy is lost by viscous friction or relaxation processes. These processes account for what is known as absorption. Another portion is scattered by the internal microstructure of the material. The combined effect of scattering and absorption is normally called attenuation.

Attenuation in a material is usually determined by evaluating the decay in amplitude (pressure that reflects into voltage) of successive back wall reflections in a

pulse-echo configuration (Larson, NDT resource center). Attenuation in bone can be described in more detail as follows. As a wave is transmitted from a fluid into bone, reflections occur at the interface. In the bone, mode conversion occurs between longitudinal and shear modes, and the mechanical wave is scattered by its complex internal microstructure (osteons and trabeculae) (Wang et al., 2010). Finally, part of the wave energy is absorbed by the bone and converted into heat.

Scattering, as defined by Nicholson, et al., (1999), refers to the change in the amplitude, frequency, velocity or direction of a wave as a result of a spatial or temporal non-uniformity of the medium. It is dependent on the number of scatterers per unit volume, their spatial distribution, size and shape, and the acoustic impedance (difference between the scatterers and the surrounding medium), (Nicholson et al., 1999).

Scattering occurs because the interfaces are smaller than the diameter of the sound beam. Then, the waves hit the boundaries of these features and scatter in directions other than its original direction of propagation. In polycrystalline materials like metals, attenuation losses result due to reflection and scattering at the grain boundaries. (Stanke and Kino, 1984; Ghoshal, 2008; Turner, 1999)

Some research can be found on the absorption of wave energy in solids, liquids and gases. When it comes to bone, it turns out to be much more difficult to model the wave propagation. Furthermore, it is a challenge to describe separately the attenuation mechanisms within the bony structures. However, it has been found that the amount of absorption in solids is not a major problem when ultrasound is used for NDT or material characterization (Carlin, 1960).

Our knowledge of absorption in biological tissue is very limited, given that the effect of absorption especially in complex non-homogeneous media is hard to separate from the scattering effect (Cobbold, 2007).

### **Total Energy Loss and Attenuation Coefficients**

During the last three decades, there has been a considerable interest in estimation of ultrasound attenuation parameters. Ultrasound attenuation can be related to intrinsic properties of the evaluated material and used for its characterization (Jirik et al., 2004). Ultrasound attenuation is particularly useful in ultrasonic imaging. Estimation of ultrasound attenuation as a function of frequency is of special importance because the energy loss can be predicted and corrected for a wide spectrum (Wilson et al., 1984).

Attenuation, as previously stated, includes the effect of absorption and scattering. It is ideally measured with a close to perfect plane wave and a coupling medium perfectly matching the impedance of the sample material. In practice, it is common to use a broadband transducer from which the attenuation for a wide frequency range is determined.

The attenuation coefficient and its dependence on frequency for biological tissues have received important attention in recent years. Although the feasibility of *in vivo* studies has been demonstrated with commercial medical evaluation devices, the majority of the data have been collected from excised specimens. The general model for attenuation coefficient indicates power law dependence with frequency such as

$$\alpha = \alpha_0 f^n, \quad (5.6)$$

where  $n$  for soft tissues varies between 1 and 2 (Cobbold, 2007).

The attenuation coefficient has more recently been measured in both cortical and cancellous bone, in an attempt to relate it to bone mineral density, bone mineral content, and physical density. In most studies  $n$  has been found to be close to 3. The usual approach has been to compare the results obtained in different bone samples (these having different densities), (Heaney et al., 1989; Laugier et al., 1993).

Attenuation coefficient vs. frequency curves for some biological tissues and water from data collected in the literature are presented in Figure 24. Note that the amount of information for skull bone at different frequencies is limited due to the fact the propagation through human skull is very difficult above  $\sim 3$  MHz.

In the present investigation, total energy loss and attenuation coefficients are determined by comparing the relative pressure drop when a piece of freshly excised skull sample is placed in a through-transmission configuration as previously detailed.



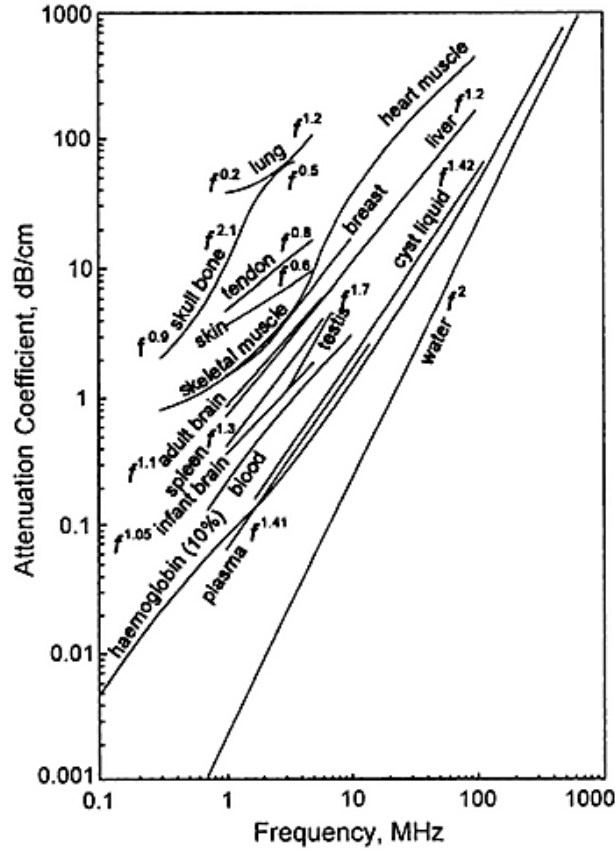


Figure 24. Attenuation coefficient in dB/cm and its frequency dependence has been determined in previous research for some biological tissues (Cobbold, 2007).

The total energy loss is defined here as the total drop in pressure caused by attenuation in the material and the loss due to reflection at the bone-water interface (see Figure 25). It will be experimentally calculated using

$$\alpha' = -\log \left( \frac{A_0(f)}{A_1(f)} \right) \frac{1}{D}, \quad (5.7)$$

where  $A_0(f)$  is the amplitude of the reference signal in the frequency domain,  $A_1(f)$  is the amplitude of the signal propagated through the material in the frequency domain, and  $D$  is the thickness of the fragment at the tested location.

The attenuation coefficient is understood as the drop in pressure caused only by the material. To account for the drop due to reflection at the bone-water interface, a transmission coefficient correction factor is introduced.

The transmission coefficient represents the fraction of energy that effectively propagates beyond the interface of two media (from material 1 into material 2). It is proportional to the speeds of propagation of sound and the density mismatch of the two materials and at normal incidence is given by

$$T^{12} = \frac{4Z_2}{(Z_1 + Z_2)} \quad , \quad (5.8)$$

where  $Z$  is the impedance of the material defined as  $Z = c\rho$ , being  $c$  and  $\rho$  the propagation sound speed and density respectively. Eq. (5.8) can be derived from Eq. (5.3) for the case of normal incidence. The transmission coefficient for angles of incidence below the first critical angle will not be frequency dependent. Therefore the same correction factor will be applied to all measurements in the experiments that satisfied the angle of incidence condition. Then, attenuation coefficient will be calculated from experimental data using

$$\alpha = - \left[ \log \left( \frac{A_1(f)}{A_0(f)} \right) + \log(1/T) \right] \frac{1}{D} \quad , \quad (5.9)$$

where

$$T = T^{wb} T^{bw} = \frac{4Z_b Z_w}{(Z_w + Z_b)^2} \quad (5.10)$$

is the transmission coefficient for a double boundary problem like the one shown in Figure 25.

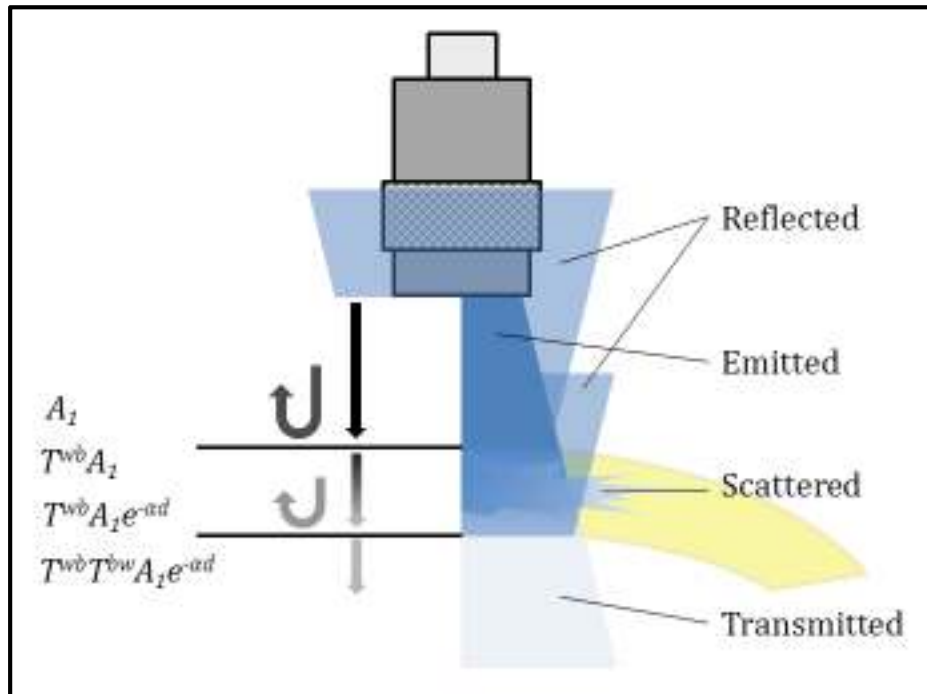


Figure 25. When the ultrasound beam encounters the water-bone interface part of the energy is reflected back to the transducer. Then, part of the energy that propagates through the material is scattered by the internal microstructure. When the wave encounters the second interface, again part of the energy is reflected. Finally, the remaining energy is effectively transmitted through the material.

## Chapter 6

# Results and Discussion

### 6.1. Wave speed

In the present study, the average group velocity for each calvarium fragment has been calculated at 0.5, 1 and 2.25 MHz. It is important to note that neither the setup used in this work, nor the ultrasonic transducers selected were optimized for wave speed measurements. The broadband transducers employed produce very short pulses (approximately 3 cycles). In this case, cross-correlation between distorted or highly attenuated pulses can lead to large errors in the measurements. The wave speed data presented are those corresponding to thick areas in the specimens where the attenuation was not too high. Despite the aforementioned limitations, it was possible to measure wave speeds for all specimens except one. The speeds of sound measured are in the range of values expected for skull bone as reported by previous groups, (Bauer et al. 2008, Wear 2000, White et al. 2006, Pichardo et al. 2010).

From the data shown in Table 6, it can be seen that from 0.5 MHz to 1 MHz, the average speed at which sound propagates through the bone layer increases for almost all the specimens. These results are in agreement with results reported by others (Bauer et al. 2008, Wear 2000, White et al. 2006, Pichardo et al. 2010). This

first increment has been described to be caused by positive dispersion in bone at low frequencies. Positive dispersion is expected for solid materials based on the casualty-induced Kramers-Kronig relations (O'Donnell and Miller, 1981). However, for 2.25 MHz it seems that the speed of sound decreases, a result that implies negative dispersion. Such phenomenon of apparent negative dispersion in highly complex materials like bone has been widely studied in previous research. As already described, unlike homogeneous media, bone is a material composed of a dense solid porous matrix filled with bone marrow (fluid). In this scenario, when both *slow* and *fast* waves propagate through the material, they may cause an apparent negative dispersion, for frequencies that have wavelengths on the order of the scatterers in the bone matrix. Bauer et al., (2008), explored the possibility that this apparent negative dispersion may be the result of interference between two propagating modes, both exhibiting positive dispersion, which would be consistent with the casualty-induced Kramers-Kronig relations. Then, this decrement in group velocity after 1 MHz may be explained by this apparent negative dispersion.

No clear correlation was found between density and wave speed. The correlation coefficients between density and wave speed in all specimens were small. This small correlation differs from what it has been previously reported (Wear et al. 2009, White et al. 2006, Pichardo et al. 2010). This lack of correlation may be due to the already established difficulty to determine precisely the speed of sound with the setup used in this study. Moreover, the density was determined as a volumetric average across the entire thickness of the specimens. Thus, what these results suggest

is that the speed of propagation of sound through the bone layer is not strongly correlated with the average volumetric density in the fragments.

Table 6. Average speed of sound through the calvarium bone layer. Estimated error for the attenuation coefficient values are shown in parenthesis ( $\pm$ ). See Appendix D for error estimation procedure.

<b>Fragment</b>	<b>0.5 MHz (<math>\pm 705</math>)</b>	<b>1 MHz (<math>\pm 388</math>)</b>	<b>2.25 MHz (<math>\pm 240</math>)</b>
I-A	2443	2405	2243
I-L			
I-R	2351	2823	2604
I-S	2633	2627	2246
II-A	2244	2266	1882
II-L	2367	2526	2032
II-P	2206	2513	2162
II-R	2457	2776	2401
II-S	2394	2547	2019
III-A	2470	2506	2064
III-L			
III-P	2660	2694	2089
III-R	2763	2822	2489
III-S	2553	2197	2273
IV-A	1987	2028	2154
IV-L	2493	2520	2404
IV-P	2295		2404
IV-R	2756	2911	2636
IV-S	2463	2555	2291

## 6.2. Attenuation coefficient

The attenuation coefficients have been determined at various locations on the specimens for 0.5, 1 and 2.25 MHz. For 5 MHz no propagated energy was effectively recorded with sufficient signal to noise. The attenuation coefficient value at the three other transducers' central frequencies was calculated for each position with the assumption of a water-bone-water propagation model, Eq. (5.9). In Figures 26-28, the steps taken for the calculation of the attenuation coefficient caused by the bone layer

are shown. First the pulses with and without the calvarium samples in the path of propagation were corrected for gain. Then, in order to obtain the frequency spectrum from the signals, a fast Fourier transform (FFT) was performed on both sample and reference pulses. Finally attenuation coefficient as a function of frequency was computed from the FFT pulses using Eq. (5.9).

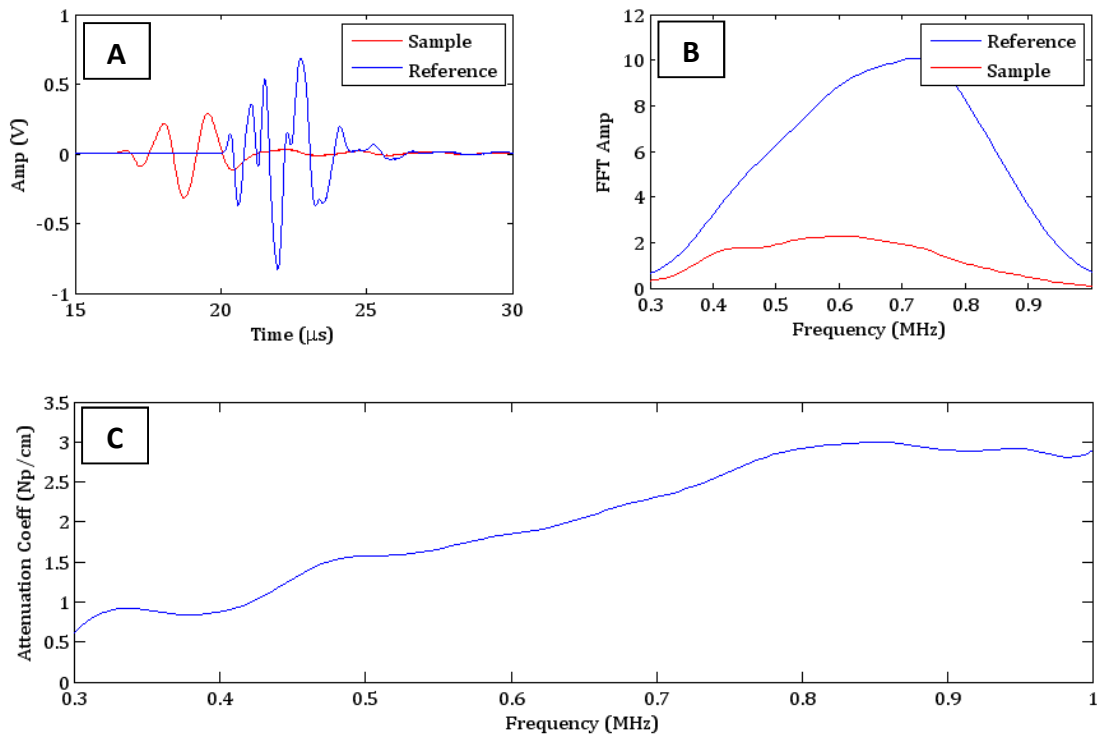


Figure 26. Procedure for calculating attenuation coefficient using 0.5 MHz signal through the calvarium samples. A: Reference pulse without calvarium sample and sample attenuated signal. B: FFT of the reference and sample signals. C: Attenuation coefficient as a function of frequency.

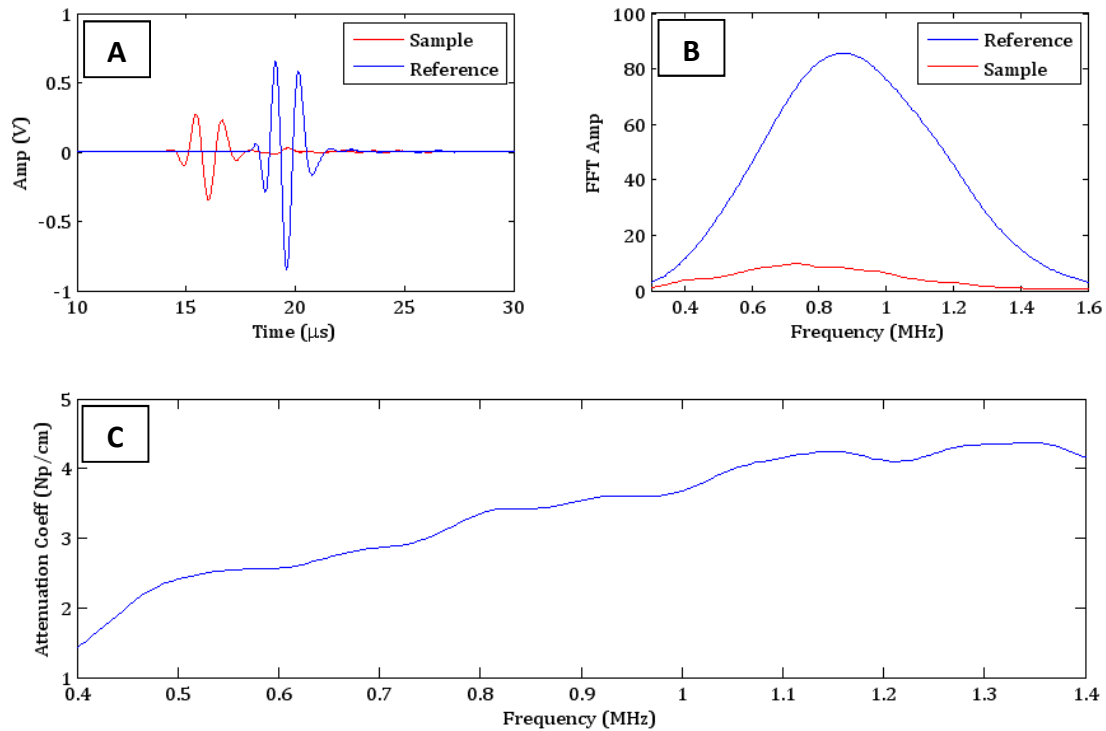


Figure 27. Procedure for calculating attenuation coefficient using 1 MHz signal through the calvarium samples. A: Reference pulse without calvarium sample and sample attenuated signal. B: FFT of the reference and sample signals. C: Attenuation coefficient as a function of frequency.

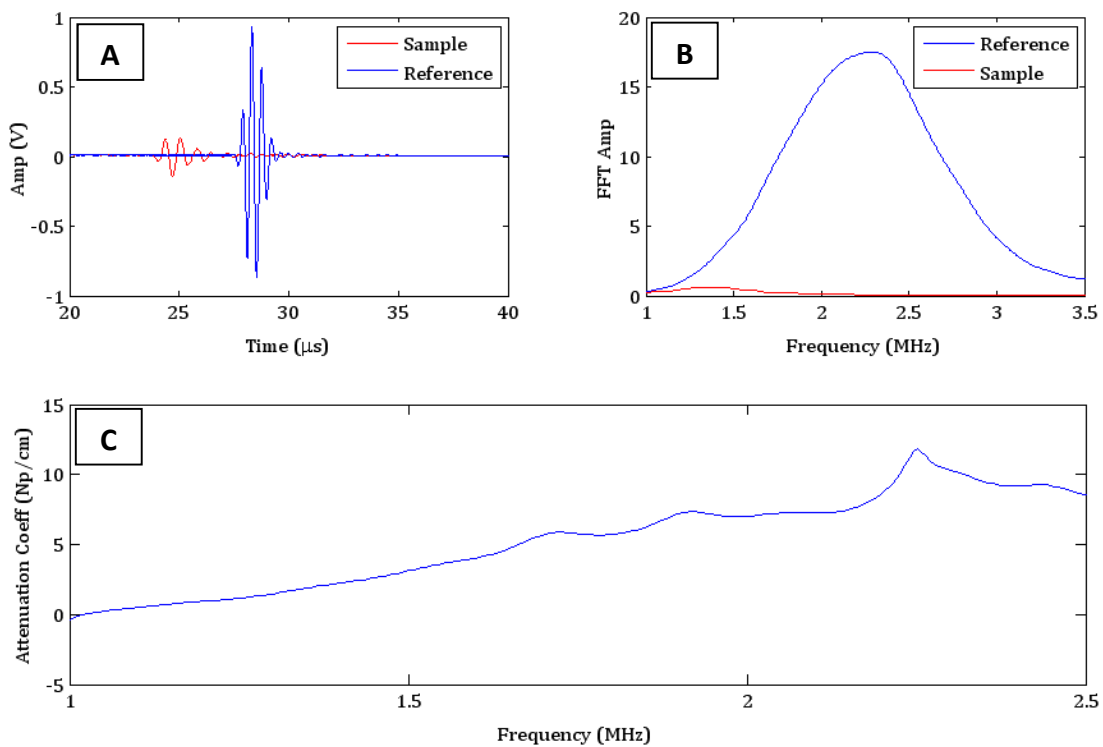


Figure 28. Procedure for calculating attenuation coefficient using 2.25 MHz signal through the calvarium samples. A: Reference pulse without calvarium sample and sample attenuated signal. B: FFT of the reference and sample signals. C: Attenuation coefficient as a function of frequency.



In the present study, rather than presenting average values of attenuation coefficient as it has been approached by previous researchers, the spatial variability of this property is fully presented. Color pictures depicting the attenuation coefficient at various locations on the specimens show well differentiated regions of high and low attenuation. These color scaled pictures shown in Fig. 29, 31, 33 and in Appendix B are shown for the rated central frequencies of the transducers (0.5, 1 and 2.25 MHz). Histograms for the same data are presented along with the color pictures. From the histograms it is easy to get a notion of the average attenuation coefficient for each specimen and frequency. Moreover, it can be seen how much the data are scattered over a wide range of values. The spatial data for the most curved specimens are limited due to the fact that fewer points satisfy the curvature condition (angle of incidence of the beam under  $20^\circ$ ). However, for all specimens but one, an important number of measurements were effectively extracted.

The first trend that can be noticed in the attenuation coefficient results, in both the color pictures and the histograms immediately below, is the increment in attenuation coefficient with increments in frequency. This dependence has been widely reported for several biological tissues in previous works (see Figure 24). Fry and Barger 1978, measured average attenuation coefficients of around 2 Np/cm at 1 MHz and between 6 and 14 Np/cm at 2.25 MHz for two heads. These values as well as the variability between donors (as it will be seen later) are in agreement with those obtained in the present work. White et al. 2006, reported lower attenuation values. This group measured attenuation coefficients ranging between 0.14 to 0.7 Np/cm for a frequency range of 0.2 to 0.9 MHz respectively. In that study, attenuation

coefficients were calculated for 10 points on 3 heads. Eight points were located in the parietal bones of the donors while two were measured from the occipital bone on one of the heads. Pichardo et al 2010, reported slightly higher values of attenuation coefficient for a similar range of frequencies. In Pichardo et al 2010, attenuation coefficients of  $0.33(\pm 0.09)$ ,  $2.40(\pm 0.09)$  and  $3.07(\pm 0.3)$  Np/cm were found for frequencies of 0.27, 0.836 and 1.402 MHz respectively.

Figs. 29-34 show the attenuation coefficients at locations on a 2D matrix for the fragments of Head II extracted from the C-scans and the histograms for these data. The rest of the matrices and histograms for all fragments studied can be found in Appendix B. The measurements in the images are separated spatially in 3 mm increments and cover a calvarium area of  $1764 \text{ mm}^2$ . The data distributions of the attenuation coefficient values are presented for fragments in Head II in Figs. 30, 32 and 34. From these histograms it is possible to notice the variability of the attenuation as well as the approximate mean value for each specimen and frequency. The variability in the attenuation coefficient data is believed to be the result of changes in the ultrasonic properties at different locations on the samples. Proof of the spatial variability hypothesis is the relatively small estimated error in the attenuation coefficient measurements (see Appendix D). Moreover, in the histograms it is clear that not only the attenuation increases with frequency but also the spatial variability is greater for higher frequencies. This dependence of both attenuation and its spatial variability with frequency can be also seen in Table 7. Although the spatial variance is so high such that the same range of attenuation coefficient values can be found for the three frequencies, a statistical analysis has demonstrated that with a confidence of

99%, all distributions are statistically different for 0.5, 1 and 2.25 MHz in the same fragment. Such increased variability at higher frequencies is likely related to variations in the specific properties of the material at the microscale as well as changes in the microstructure. As already stated, the mean volumetric density, at different locations of the specimens, varies greatly along the surface of the samples (see Figure 16). It is also expected that the microstructure shows the same level of variability across the volume of the samples.

Table 7. Mean and spatial variation of attenuation coefficient values for all fragments studied at 0.5, 1 and 2.25 MHz. Estimated error for the attenuation coefficient values are shown in parenthesis ( $\pm$ ). See Appendix D for error estimation procedure.

Sample	0.5 (MHz)		1 (MHz)		2.25 (MHz)	
	Mean (Np/cm) ( $\pm 0.30$ )	Variance (Np/cm)	Mean (Np/cm) ( $\pm 0.33$ )	Variance (Np/cm)	Mean (Np/cm) ( $\pm 0.37$ )	Variance (Np/cm)
I-A	2.8	1.8	6.2	3.6	13.9	13.204
I-L						
I-P						
I-R	2.6	4.8	6.2	5.7	10.9	9.8
I-S	2.6	3.4	5.6	6.2	10.0	13.9
II-A	3.8	3.9	6.8	9.2	9.8	15.6
II-L	3.6	2.2	7.4	7.8	11.6	16.3
II-P	2.9	1.6	7.4	8.6	11.1	13.3
II-R	4.5	2.6	8.6	5.7	12.3	9.9
II-S	2.3	1.1	5.4	4.0	9.2	7.2
III-A	3.2	1.5	5.9	3.6	8.6	4.2
III-L						
III-P	3.2	1.4	5.0	2.2	8.0	4.2
III-R	2.4	1.3	4.2	1.9	7.3	5.1
III-S	2.6	0.6	4.6	3.0	6.3	6.7
IV-A	1.0	0.4	3.7	2.1	7.2	6.5
IV-L	1.8	0.8	4.3	4.5	7.5	9.6
IV-P	1.9	1.6			6.0	7.2
IV-R	0.9	0.8	4.1	2.4	7.1	5.2
IV-S	1.7	1.3	4.2	3.0	7.5	7.8

A student's t-test was performed on the mean values of attenuation coefficient in all fragments and frequencies. The results suggest a higher variability of attenuation between donors and even between fragments in the same head. Two of the four heads (head I and head IV) showed lower variability and presented mean attenuation values statistically comparable between some fragments at the three frequencies. The conclusions obtained from the t-test for these two *more attenuation-homogenous* heads are presented in Appendix C. Higher variability of attenuation coefficient values was encountered in fragments of heads II and III. Furthermore, even higher variability was found between the same regions in different heads. These results confirm that variations in attenuation coefficient can be expected for different locations in the same head and much more in calvaria from different donors.

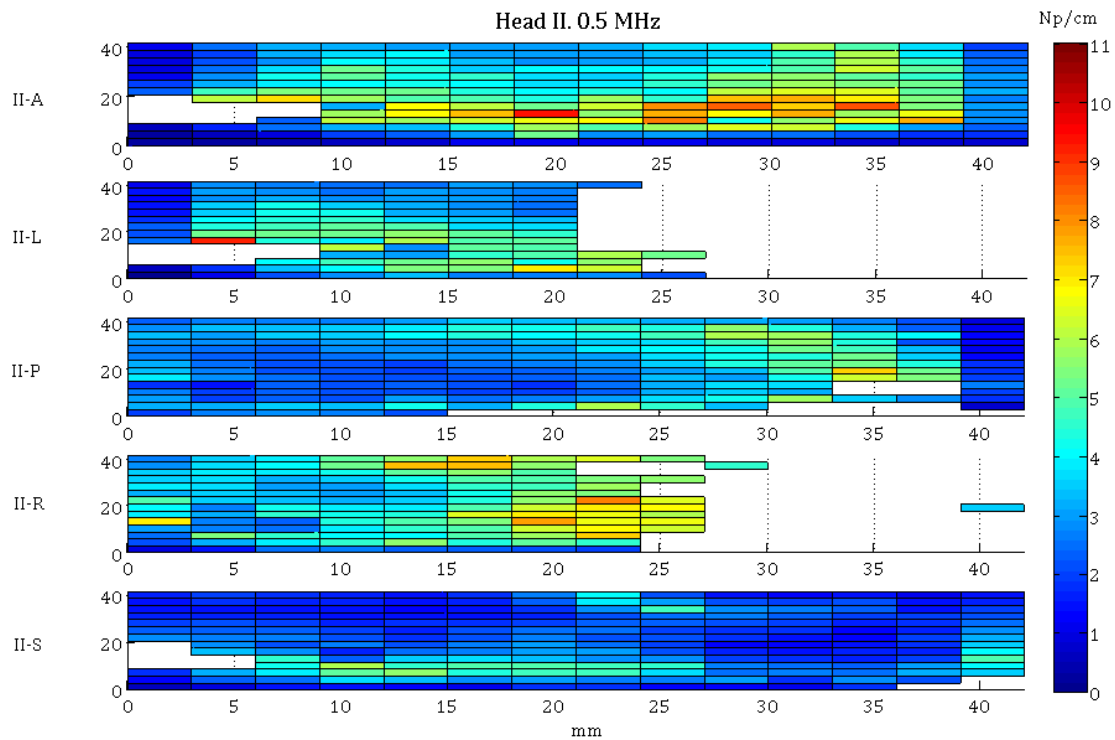


Figure 29. 2-D color images show regions of high and low attenuation for the five fragments excised from head I at 0.5 MHz.

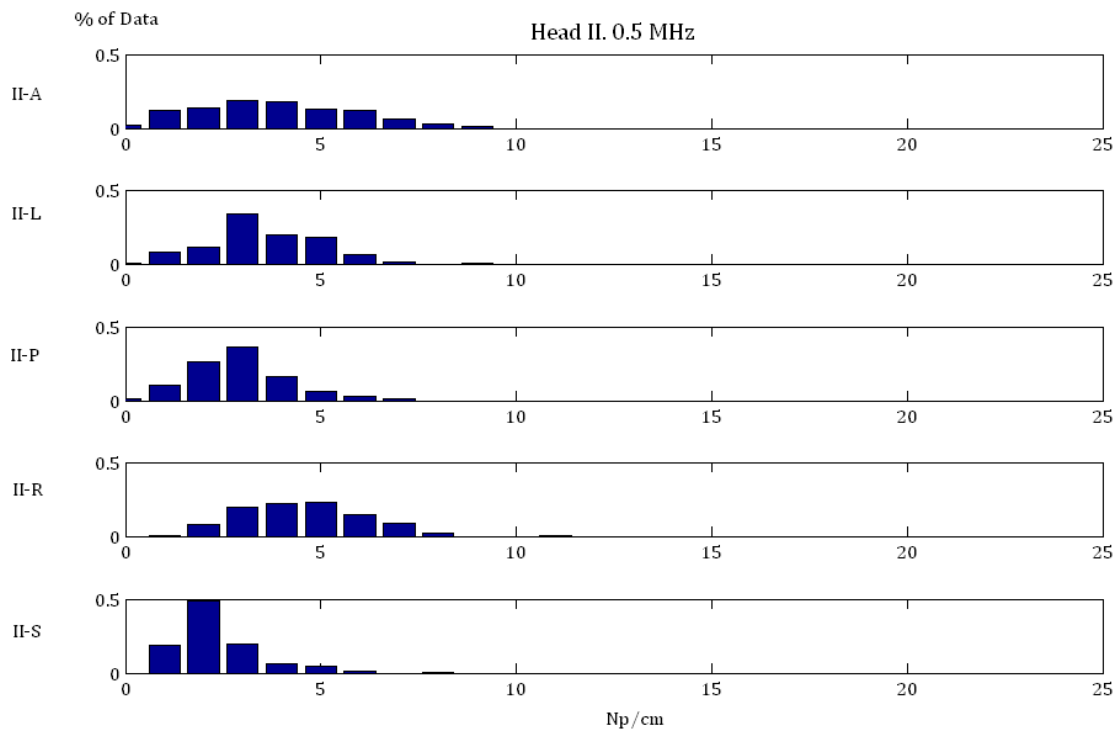


Figure 30. Histograms computed from attenuation coefficient data show the spatial variability of attenuation values for the five fragments excised from head I at 0.5 MHz.

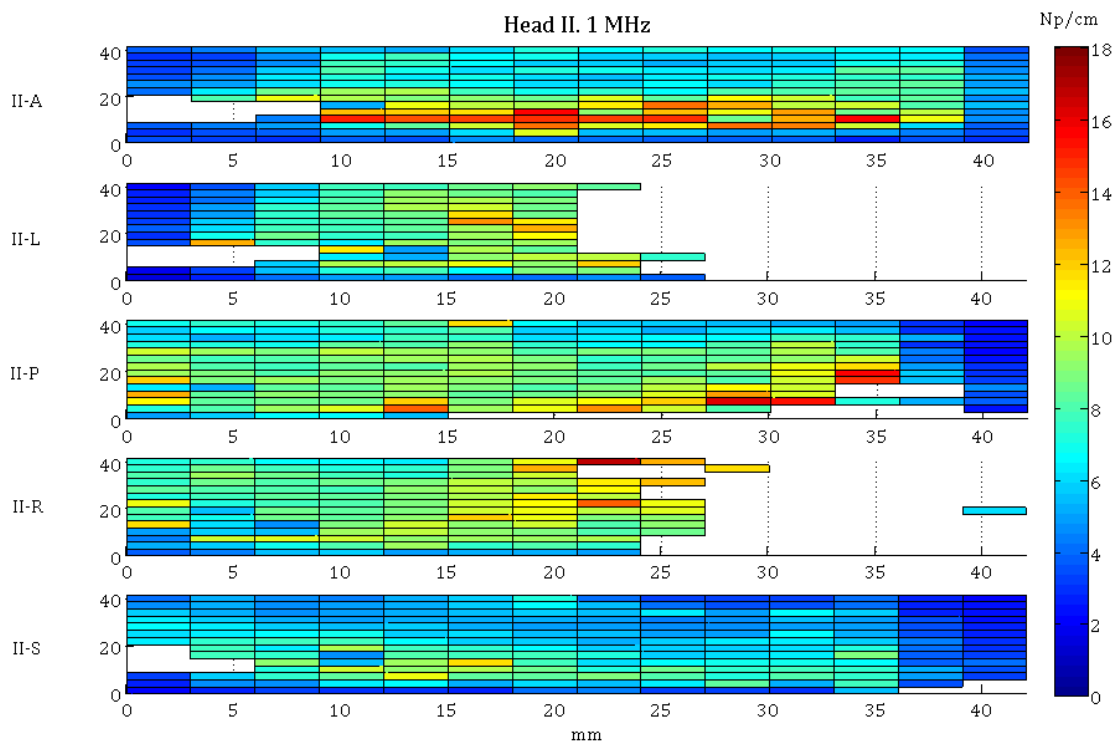


Figure 31. 2-D color images show regions of high and low attenuation for the five fragments excised from head I at 1 MHz.

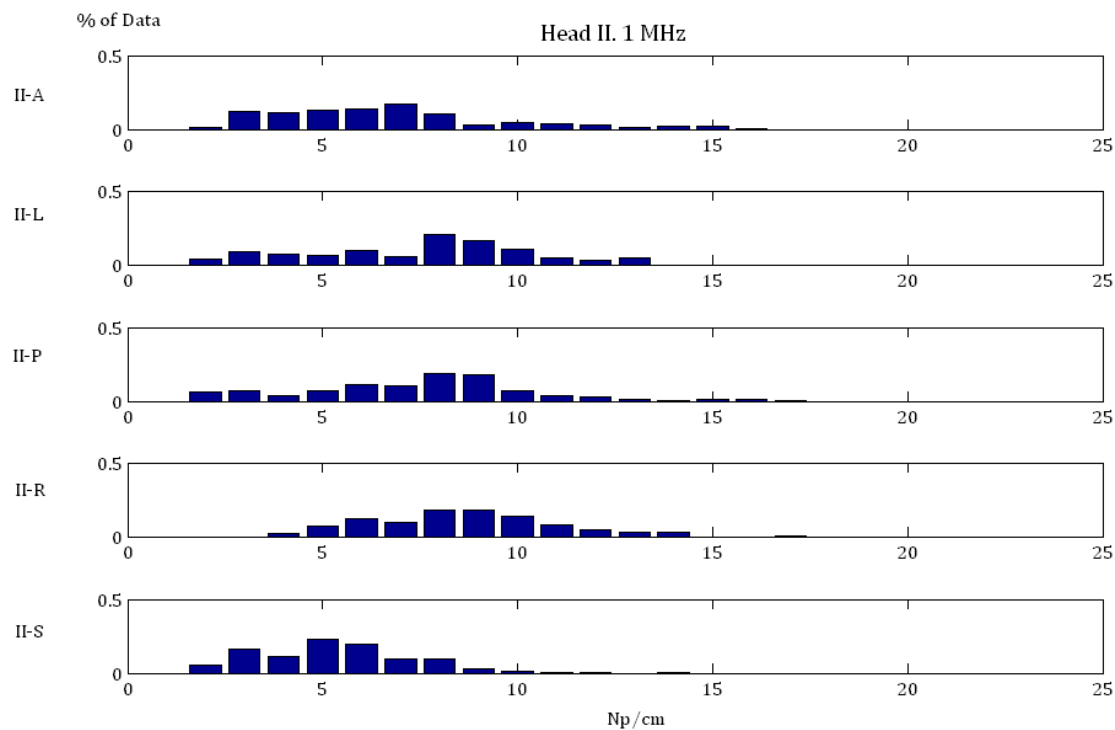


Figure 32. Histograms computed from attenuation coefficient data show the spatial variability of attenuation values for the five fragments excised from head I at 1 MHz.

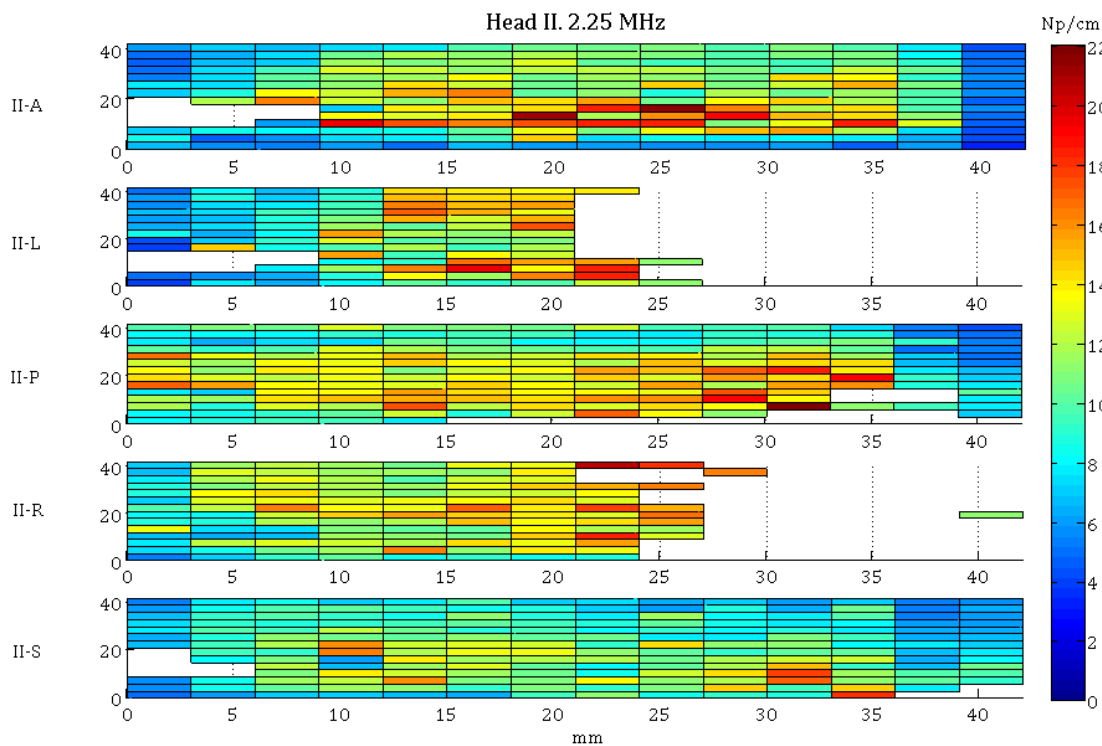


Figure 33. 2-D color images show regions of high and low attenuation for the five fragments excised from head I at 2.25 MHz.

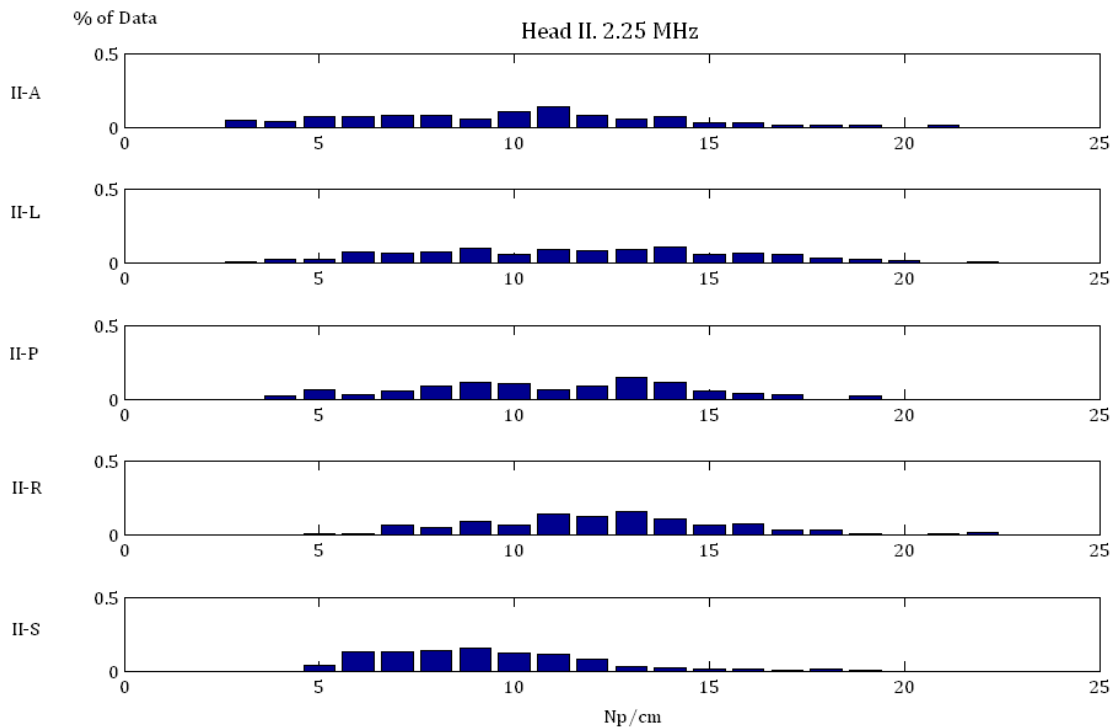


Figure 34. Histograms computed from attenuation coefficient data show the spatial variability of attenuation values for the five fragments excised from head I at 2.25 MHz.

The correlation between mean volumetric density and mean attenuation coefficient for all fragments is shown in Fig. 35. The data in the plot have been fit assuming a linear correlation. From the  $R^2$  it is possible to see a greater correlation between mean volumetric density and attenuation coefficient at higher frequencies. In Pichardo et al 2010, through a multilayer model, curves were generated that represented the behavior of the attenuation well as a function of density in the data collected in the study. However, the authors did not find on average a significant difference between low density and high density bone for low frequencies. On the contrary, for higher frequencies (frequencies closer to 1.4 MHz) the attenuation for both cortical (high density) and trabecular (low density) bone showed some correlation with density. Such increased correlation between density and attenuation for higher frequencies is in agreement with the results obtained in the present study. These results suggest that attenuation at higher frequencies is more strongly influenced by changes in the microstructure of the bone, which is closely related to density.



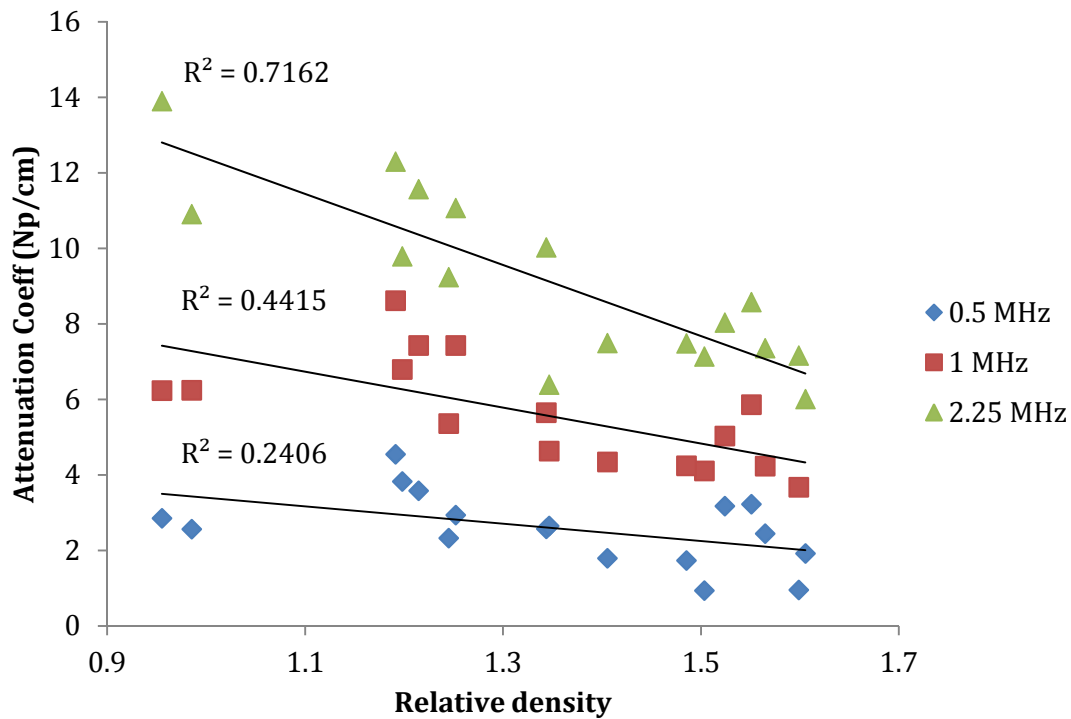


Figure 35. Correlation between mean volumetric density and mean attenuation coefficient for all fragments at frequencies of 0.5, 1 and 2.25 MHz. The estimated error for the attenuation coefficient values were,  $\pm 0.30$  at 0.5 MHz,  $\pm 0.33$  at 1 MHz, and  $\pm 0.37$  at 2.25 MHz. See Appendix D for the error estimation procedure.

## Chapter 7

# Conclusions and Future Work

In this thesis, experimental equipment and protocols have been established for measurement of speed of sound and attenuation coefficient on human calvarium fragments under *ex-vivo* conditions.

A pulse-echo propagation configuration has been effectively employed to obtain thickness and curvature of excised human calvarium fragments. These thickness and curvature data have been later used to calculate ultrasonic properties of skull bone. From thickness data, great variability of the thickness in even small regions in the calvarium fragments can be seen.

From through-transmission pulses propagated through human calvaria, along with thickness data from pulse-echoes, the speed of sound has been determined at multiple locations on the samples. Some limitations of thickness and angle of incidence have been encountered such that calculations of sound speed from through-transmission pulses in human calvaria were difficult. However, average speeds of sound for the eighteen fragments were obtained and the values were in agreement with those reported by previous authors.

Attenuation of ultrasound in human calvaria has been assessed at frequencies of 0.5, 1 and 2.25 MHz at various locations on the samples. The attenuation coefficients have been obtained from the measurements of pressure drop in multiple locations on the total of eighteen samples from four head donors. Moreover, the spatial variation of the attenuation coefficient has been explored from the numerous data extracted from the experiments. The attenuation coefficient data distributions for the eighteen fragments at the same frequencies were obtained. These histograms along with the results of a t-test performed on the data suggest that the attenuation coefficient varies spatially much more than expected. Additionally, a high variation of attenuation coefficients can be expected in calvaria from different donors. Furthermore, such spatial variation seems to increase with frequency for the three frequencies studied, indicating an increased sensitivity of attenuation with changes in the microstructure of bone.

Quantitative densitometry has also been performed on the human calvarium samples. Polymer phantoms have been used as density references during the computed tomography sessions. Bone density information has been obtained from computed tomography images through an adapted Matlab code. Average volumetric densities have been correlated with the ultrasonic properties. No strong correlation between mean volumetric density and speed of propagation of sound through calvarium bone has been found. On the contrary, attenuation coefficient, especially for higher frequencies, shows some correlation with mean volumetric density. This result again suggests a stronger sensitivity of attenuation in calvarium with changes in the microstructure that are related to density.

From the results obtained in the present work, it can be concluded that the statistics of the variation of the ultrasonic properties of calvarium for different frequencies, locations and donors, have to be considered in computational and analytical models of this phenomenon. A realistic model of the propagation of ultrasound through calvarium should replicate the behavior described here. Moreover, future research should explore practical experiments that can be performed *in-vivo* and provide information to predict the speed of sound, attenuation coefficient and its variability at different locations of the calvarium. Thus, diffuse ultrasonic backscatter may be used to obtain scattering information that can be related to speed of sound and attenuation coefficient.

# Bibliography

Aaslid, R., Markwalder, T., and Nornes, H. (1982). Noninvasive transcranial doppler ultrasound recording of flow velocity in basal cerebral arteries. *Journal of Neurosurgery*, 57(6), 769–74.

Aggelis, D. G. and Shiotani, T. (2007). Repair evaluation of concrete cracks using surface and through-transmission wave measurements, cement and concrete composites. *Cement and Concrete Composites*, 29(9), 700-711.

Aubry, J. F., Tanter, M., Pernot, M., Thomas, J. L., and Fink, M. (2003). Experimental demonstration of noninvasive transskull adaptive focusing based on prior computed tomography scans. *Journal of the Acoustical Society of America*, 113(1), 84-93.

Azhari, H. (Ed.). (2010). *Basics of Biomedical Ultrasound for Engineers*. New Jersey: John Wiley and Sons, Inc.

Bankman, I. (2003). *Handbook of Medical Imaging: Processing and Analysis Management (Biomedical Engineering)* (1st ed.) San Diego, CA: Academic Press.

- Bauer A., Marutyan K., Holland M. R and Miller J.G. (2008). Negative Dispersion in bone: the role of interference in measurements of the apparent phase velocity of two temporally overlapping signals. *Journal of the Acoustical Society of America*, 123 2407-14
- Brunader, R., and Shelton, D. (2002). Radiologic bone assessment in the evaluation of osteoporosis. *American Family Physician*, 65(7), 1357-1365.
- Carlin, B. (1960). *Ultrasonics*. (Second ed., ). New York: McGraw-Hill Book company.
- Cartz, L. (1995). *Nondestructive Testing: Radiography, Ultrasonics, Liquid Penetrant, Magnetic Particle, Eddy Current* ASM International.
- Centers for Disease Control and Prevention. (2003). *Explosions and Blast Injuries: A Primer for Clinicians*. Retrieved 09/10/2011, 2011, from <http://emergency.cdc.gov/masscasualties/explosions.asp>
- Chen, C. H. (2007). *Ultrasonic and Advanced Methods for Nondestructive Testing and Material Characterization*. Singapore: World Scientific Publishing Co.
- Christopher, F. N., Hans D., Fuerst T., Gluer C., Genant H. (1999). *Quantitative Ultrasound. Assessment of Osteoporosis and Bone Status*. New York: Martin Dunitz.

- Clement, G. T., White, P. J., and Hynynen, K. (2004). Enhanced ultrasound transmission through the human skull using shear mode conversion. *Journal of the Acoustical Society of America*, 115(3), 1356-1364.
- Cobbold, R. S. C. (2007). *Foundations of biomedical ultrasound*. Oxford: Oxford University Press.
- Digital imaging and communications in medicine (DICOM) part 10: Media storage and file format for media interchange (2007). *National Electrical Manufacturers Association*.
- Erasmus MC. *Superharmonic imaging*. Retrieved 09/22/2011, 2011, from <http://www.erasmusmc.nl/BME/944895/transducers/1891935/superharmonic>
- Feeman, T. G. (2010). *Mathematics of Medical Imaging: A Beginner's Guide* (1st edition ed.). Villanova, PA: Springer.
- Fred E. Stanke and G. S. Kino. (1984). A unified theory for elastic wave propagation in polycrystalline materials. *Journal of the Acoustical Society of America*, 75 (3), 665-681.
- Fry, F. J., and Barger, J. E. (1978). Acoustical properties of the human skull. *Journal of the Acoustical Society of America*, 63(5), 1576-1590.
- Fry, F. (1977). Trans-skull transmission of an intense focused ultrasonic beam. *Ultrasound in Medicine and Biology*, 3, 179-84.

- Ghoshal, G. (2008). *Diffuse Ultrasonic Scattering in Heterogeneous Media*. Ph.D. dissertation. University of Nebraska-Lincoln.
- Heaney R. P., Avioli L.V., Chesnut C. H., Lappe J., Recker R. R., Brandenburger G. H. (1989). Osteoporotic bone fragility. Detection by ultrasound transmission velocity. *Journal of the American Medical Association*, 261(20), 2086-90.
- Hernot, S., and Klibanov, A. (2008). Microbubbles in ultrasound-triggered drug and gene delivery.. *Advanced Drug Delivery Reviews*, 60(10), 1153-66.
- Hsieh, J. (2003). *Computed Tomography: Principles, Design, Artifacts, and Recent Advances*. Bellingham, Washington: The Society of Photo-Optical Instrumentation Engineers.
- Jirik, R., Taxt, T., and Jan, J. (2004). Ultrasound attenuation imaging. *Journal of Electrical Engineering*, 55(7-8), 180-187.
- Kinoshita, M., McDannold, N., Jolesz, F. A., and Hynynen, K. (2006). Targeted delivery of antibodies through the blood-brain barrier by MRI-guided focused ultrasound. *Biochemical and Biophysical Research Communications* 340, 1085–90.
- Larson, B. *NDT resource center*. Retrieved 09/15, 2011, from <http://www.ndt-ed.org/EducationResources/CommunityCollege/Ultrasonics/Physics/attenuation.htm>



- Laugier, P., Giat, P., and Berger, G. (1993). Broadband ultrasonic attenuation imaging: A new imaging technique of the os calcis. *Calcified Tissue International*, 54(2), 83-86.
- Ling, G., Bandak, F., Armonda, R., Grant, G., and Ecklund, J. (2009). Explosive blast neurotrauma. *Journal of Neurotrauma*, 26(6), 815-25.
- Lionetto, F., Montagna, F., and Maffezzoli, A. (2005). Ultrasonic dynamic mechanical analysis of polymers. *Applied Rheology* 15(5), 326-335.
- Marquet, F., Hynynen, K., Teichert, T., Ferrera, V., and Konofagou, E. (2011). Noninvasive, transient and selective blood-brain barrier opening in non-human primates in vivo. *PLoS ONE*, 6(7).
- Nicholson, P. H. F., Strelitzki, R., Cleveland, R. O., and Buxsein, M. L. (1999). Scattering of ultrasound in cancellous bone: Predictions from a theoretical model. *Journal of Biomechanics*, 33(4), 503-506.
- O'Donnell, M., Jaynes, E. T., Miller, J. G. (1981). Kramers-Kronig relationship between ultrasonic attenuation and phase velocity. *Acoustical Society of America* 69, 696-701
- Olympus. Inspection and Measurement Systems. *Immersion transducers*. Retrieved 01/02, 2011, from <http://www.olympus-ims.com/en/ultrasonic-transducers/immersion/>

- Papadakis, E. P. (1999). *Ultrasonic Instruments and Devices*. San Diego, CA: Academic Press.
- Pearson Education Inc. publishing as Benjamin Cummings. *Skull Bones*. Retrieved 01/15, 2012 from [http://www.pearsoned.co.uk/Imprints / Benjamin Cummings/](http://www.pearsoned.co.uk/Imprints/BenjaminCummings/)
- Pichardo, S., Sin, V. W., and Hynynen, K. (2011). Multi-frequency characterization of the speed of sound and attenuation coefficient for longitudinal transmission of freshly excised human skulls. *Physics in Medicine and Biology*, 56(1), 219–250.
- Raj, B., Rajendran, V., and Palanichamy, P. (2004). *Science and Technology of Ultrasonics*. Tamilnadu, India: Alpha Science Int'l Ltd.
- Rice D. (Ed.). (2008). *Craniofacial Sutures: Development, Disease and Treatment*. London: S. Karger AG.
- Ries, F. (1997). Clinical experience with echo-enhanced transcranial doppler and duplex imaging. *Journal of Neuroimaging* 1, 15-21.
- Rustgi, S., Siegel, J., Braunstein, M., Craven, J., and Greenfield, M. (1980). Accuracy of bone mineral data. *American Journal of Roentgenology*, 135(2), -275-277.
- Schmerr, L. W., and Song, S. (2007). *Ultrasonic Nondestructive Evaluation Systems: Models and Measurements* (1st ed.). Ames, IA: Springer.

- Sekhon, K., Kazakia, G. J., Burghardt, A. J., Hermannsson, B., and Majumdar, S. (2009). Accuracy of volumetric bone mineral density measurement in high-resolution peripheral quantitative computed tomography. *Bone*, 45(3), 473-479.
- Smith, F. P. (2001). *Neurology and Neurosurgery. Basic Principles* (1st edition ed.) Rochester, NY: University of Rochester Press.
- Turner, J. A. (1999). Elastic wave propagation and scattering in heterogeneous, anisotropic media: Textured polycrystalline materials. *Journal of the Acoustical Society of America* 106(2), 541-552.
- Wang, X., Nyman, J. S., Dong, X., Leng, H., and Reyes, M. (2010). Fundamental biomechanics in bone tissue engineering. *Synthesis Lectures on Tissue Engineering*, 2(1), 1-225.
- Wear, K. A. (2000). Measurements of phase velocity and group velocity in human calcaneus. *Ultrasound in Medicine and Biology* 26, 641-6.
- Wear, K. A. (2008). Ultrasonic scattering from cancellous bone: A review. *Ultrasonics*, 55(7), 1432-1441.
- White, P. J., Wardlaw, J., and Easton, V. (2000). Can noninvasive imaging accurately depict intracranial aneurysms? A systematic review. *Radiology*, 217(2), 319-20.
- White P. J., Clement G. T., Hynynen K. (2006) Longitudinal and shear mode ultrasound propagation in human skull bone. *Ultrasound in Medicine and Biology*, 32 1085-96

Wilson, L. S., Robinson, D. E., and Doust, B. D. (1984). Frequency domain processing for ultrasonic attenuation measurement in liver. *Ultrasonic Imaging*, 6(3), 278-292.

Zunker, P., Wilms, H., Brossmann, J., Georgiadis, D., Weber, S., and Deuschl, G. Echo Contrast-Enhanced transcranial ultrasound. frequency of use, diagnostic benefit, and validity of results compared with MRA. *Stroke*, 33(11), 2600-3

# Appendix A

Matlab code for mean volumetric density determination at different locations on the calvarium fragments from raw DICOM images data

```

I=2370; %I: identity number of initial slice
F=2568; %F: identity number of final slice
q=F-I;
%Loading 3D array with 2D slices
for i=1:q
    l=I;
    l=l+i;
    if l<=9
        sample(:,i)=int16(dicomread(['IN00000' int2str(l)]));
    end
    if l<=99 && l>9
        sample(:,i)=int16(dicomread(['IN0000' int2str(l)]));
    end
    if l>99 && l<=999
        sample(:,i)=int16(dicomread(['IN000' int2str(l)]));
    end
    if l>999 && l<=9999
        sample(:,i)=int16(dicomread(['IN00' int2str(l)]));
    end
end
sample=sample-1024; %Intercept correction
%Normalization of low density pixels
A=(sample<=-700);
sample(A)=-1024;
[~,~,n]=size(sample);
%Defining step sizes (3 mm x 3 mm areas)
%Slices spaced at 0.625 mm
%Pixsize: Pixel size that varies for each calvarium fragment
r1=round(3/pixsize);
r2=round(3/0.625);
t=zeros((512/r1),(n/r2));
s=zeros((512/r1),(n/r2));
%Loading thickness and density matrices
for j=1:r1:(512-r1)
    for k=1:r2:(n-r2)
        b=0;
        c=0;
        for i=1:508
            if mean(mean(mean(sample(i:i+3,j:j+r1-1,k:k+r2-1))))~-1024 && b==0 && i<=508

```

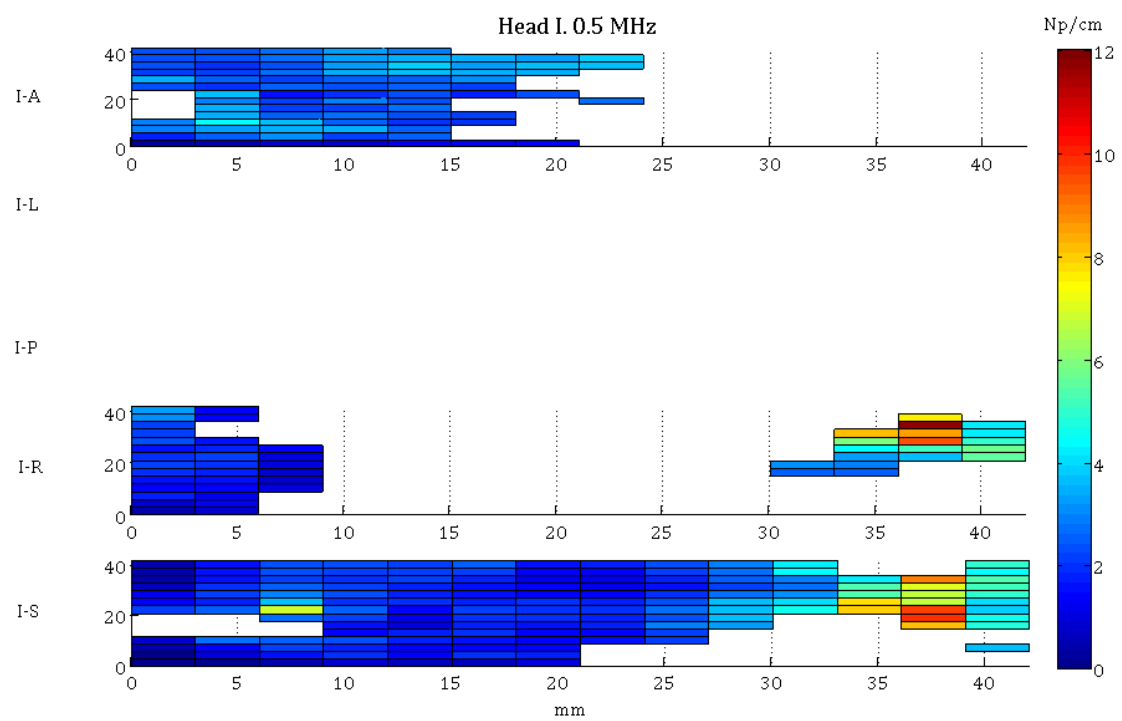
```

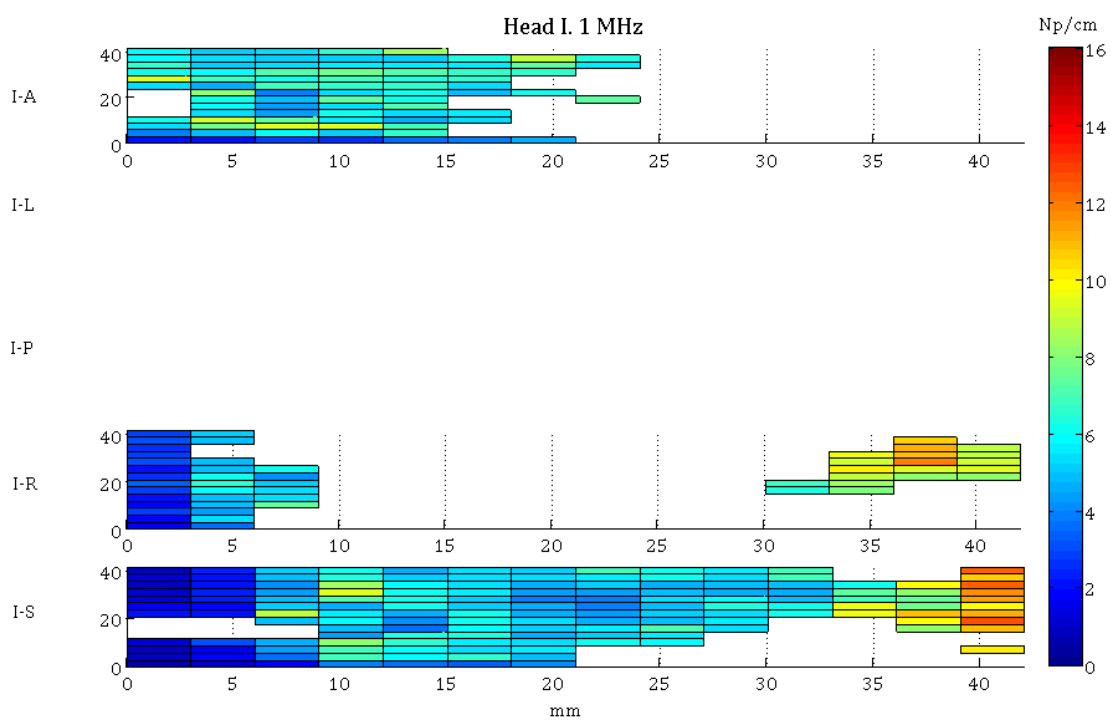
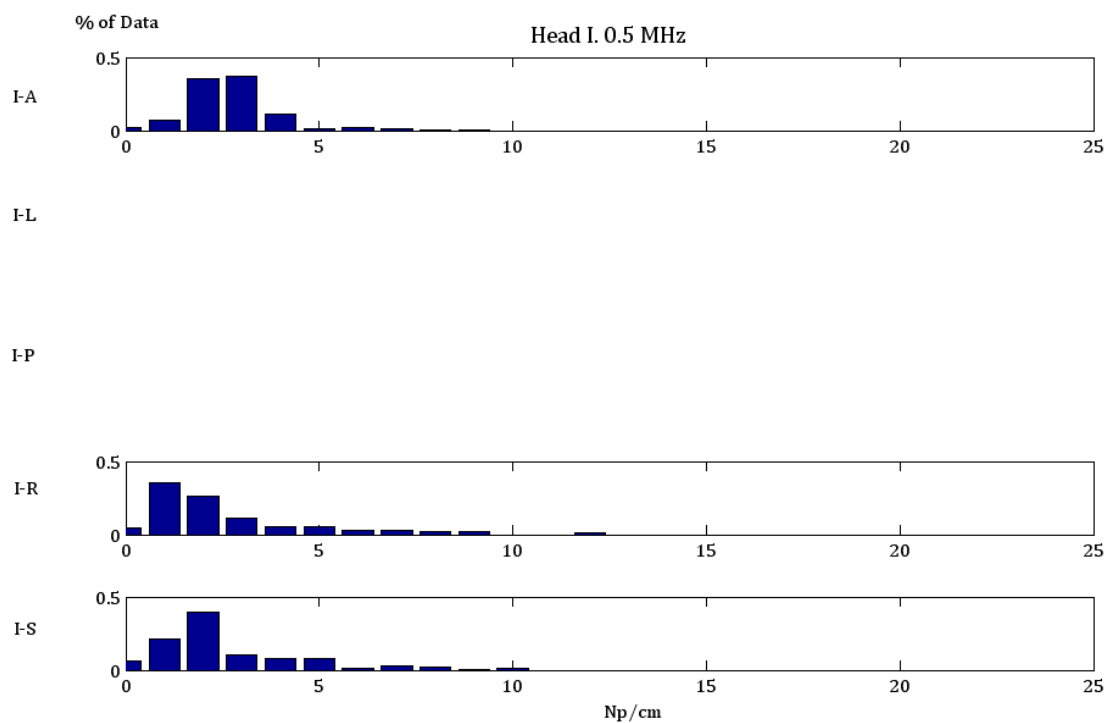
while mean(mean(mean(sample(i:i+3,j:j+r1-1,k:k+r2-1))))~-1024 && b==0 && i<=508
    t((j+r1-1)/r1,(k+r2-1)/r2)=t((j+r1-1)/r1,(k+r2-1)/r2)+1;
    s((j+r1-1)/r1,(k+r2-1)/r2)=s((j+r1-1)/r1,(k+r2-1)/r2)+mean(mean(sample(i,j:j+r1-1,k:k+r2-
1)));
    i=i+1;
end
b=1;
end
end
end
end
end
%Volumetric mean Density and Thickness matrices
%Matrices flipped to match order of ultrasonic data acquisition
d=fliplr((s./t));
t=fliplr(t*pixsize);

```

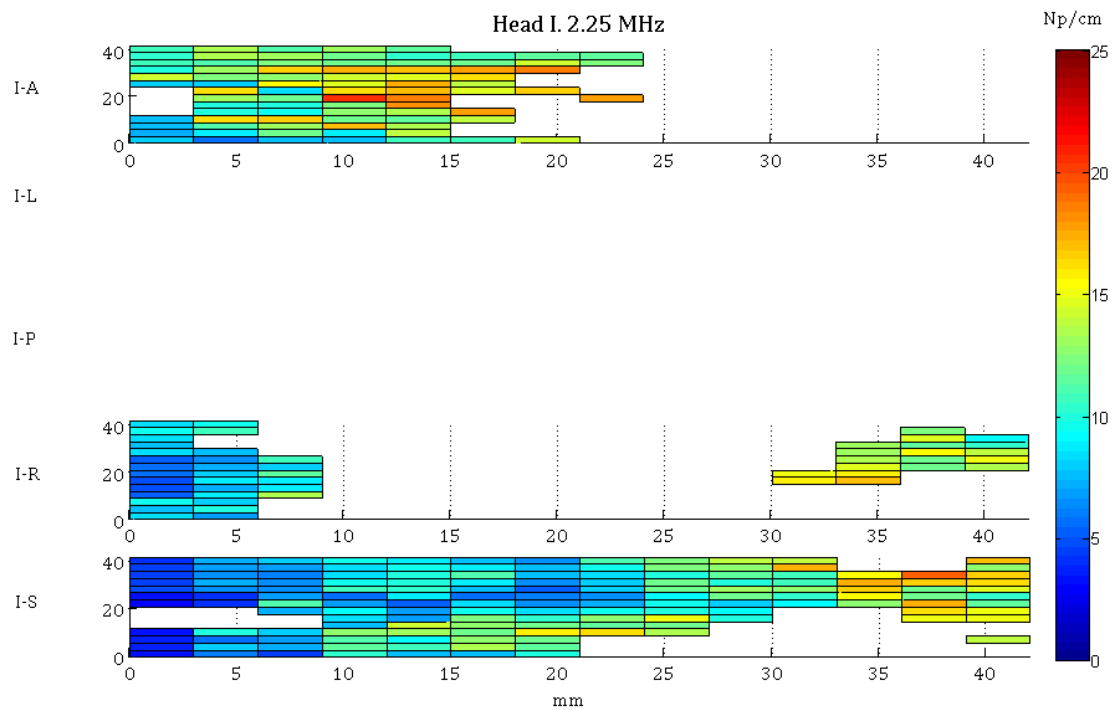
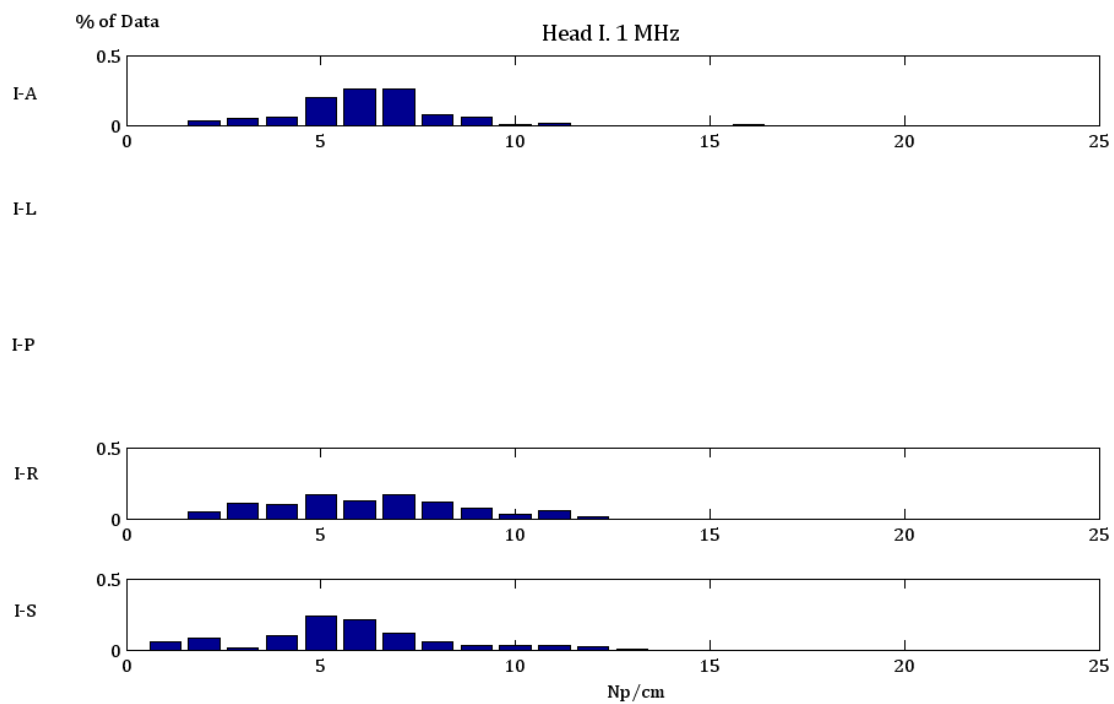
# Appendix B

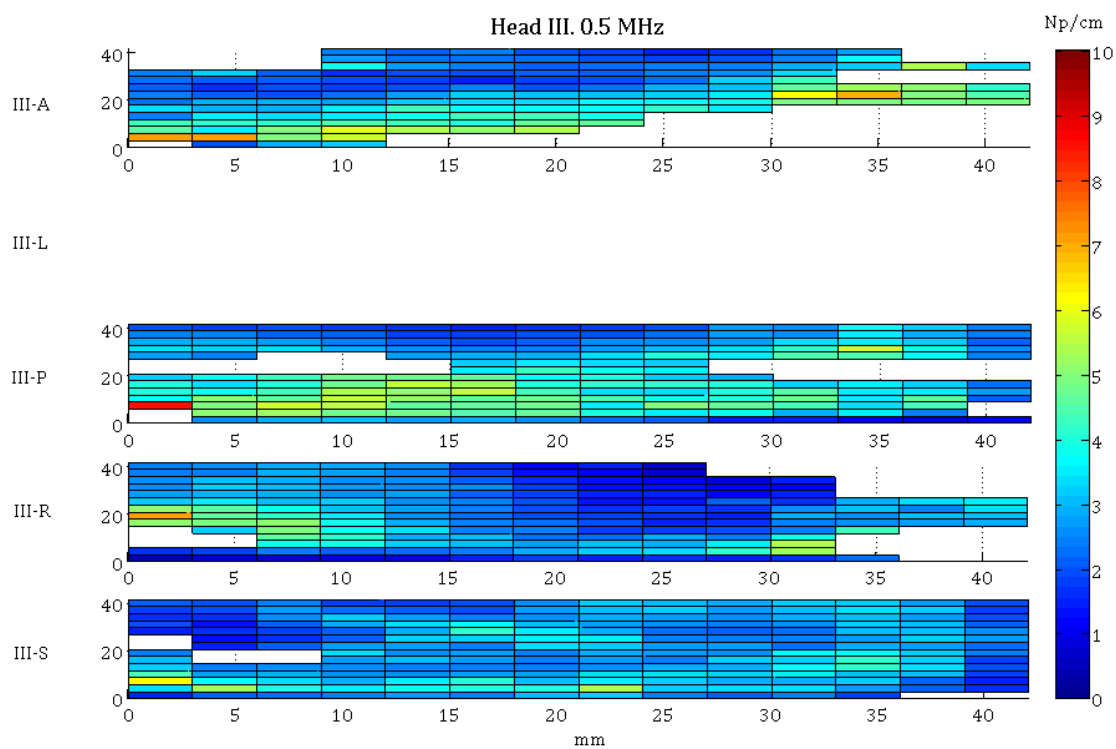
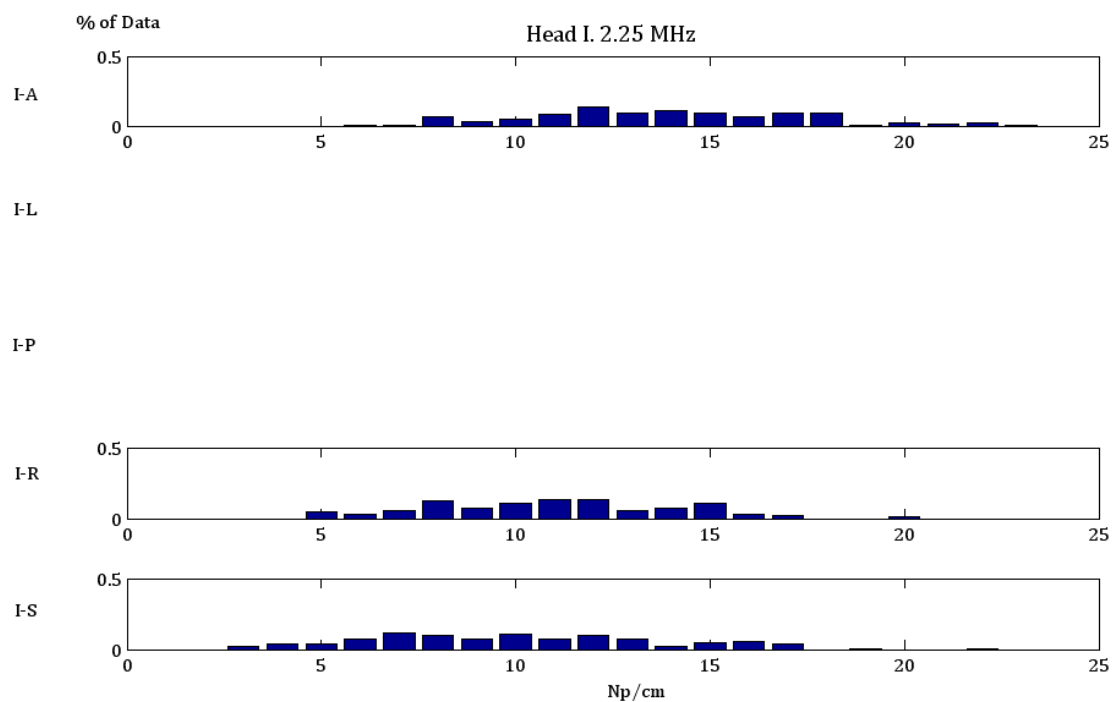
Spatial variability of the ultrasonic attenuation coefficient at 0.5, 1 and 2.25 MHz for the freshly-excised human calvarium samples taken from Heads I, III and IV are presented in the following figures.

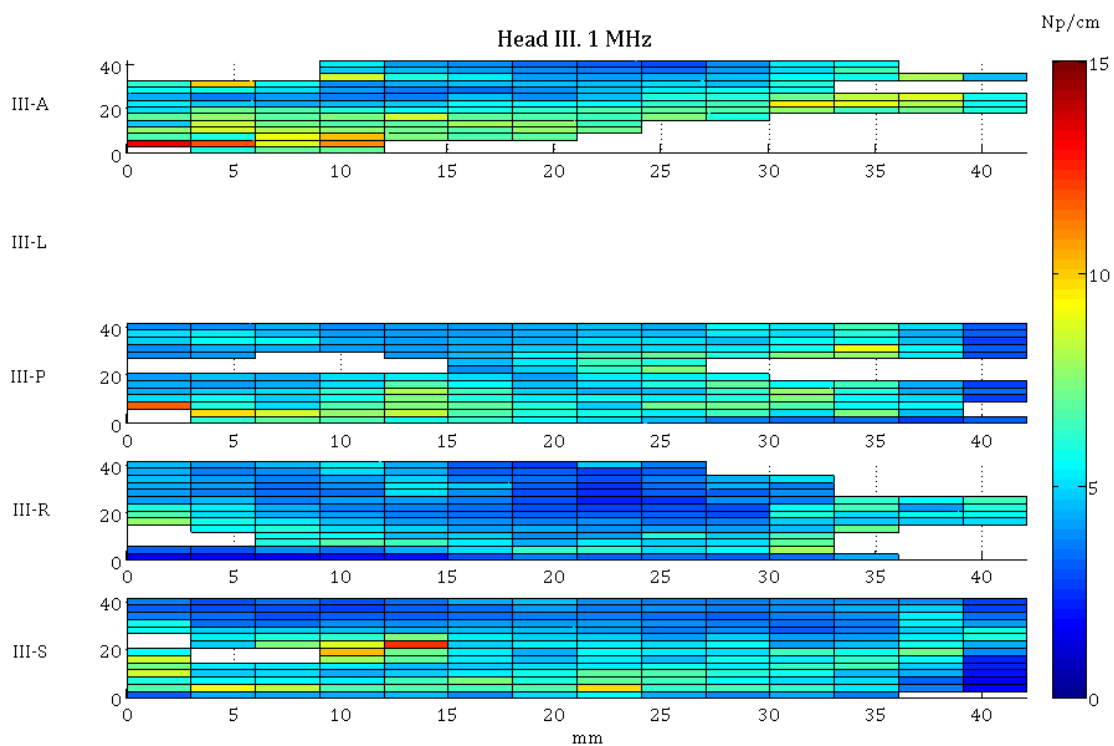
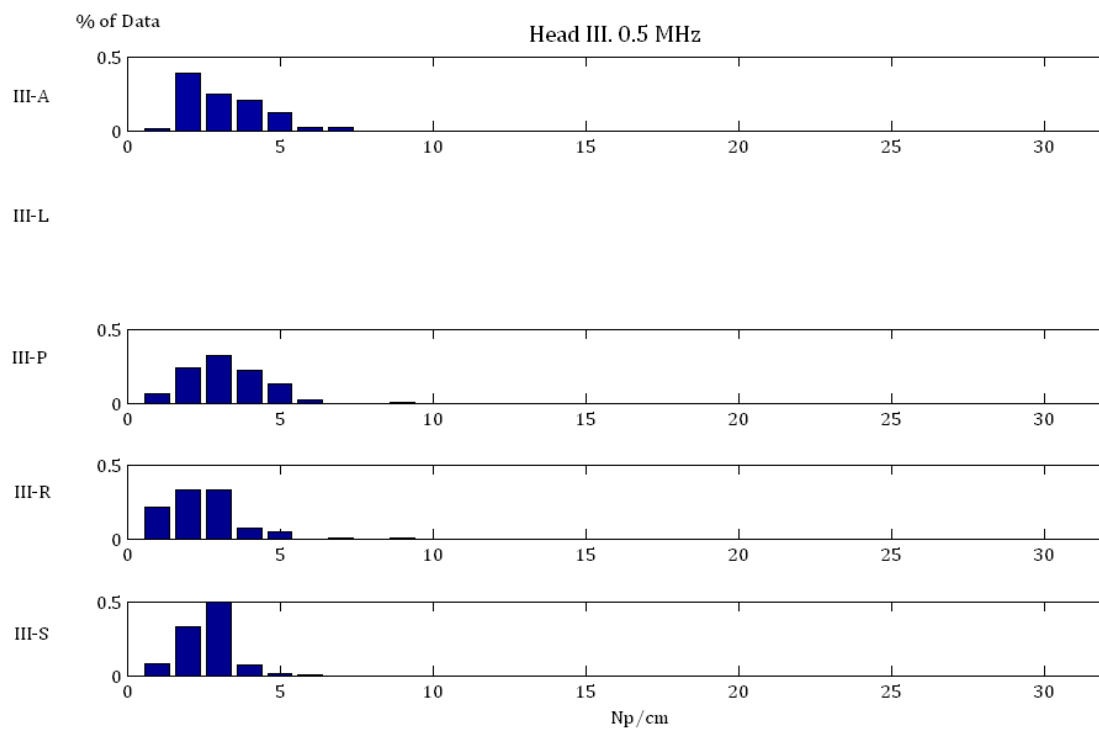


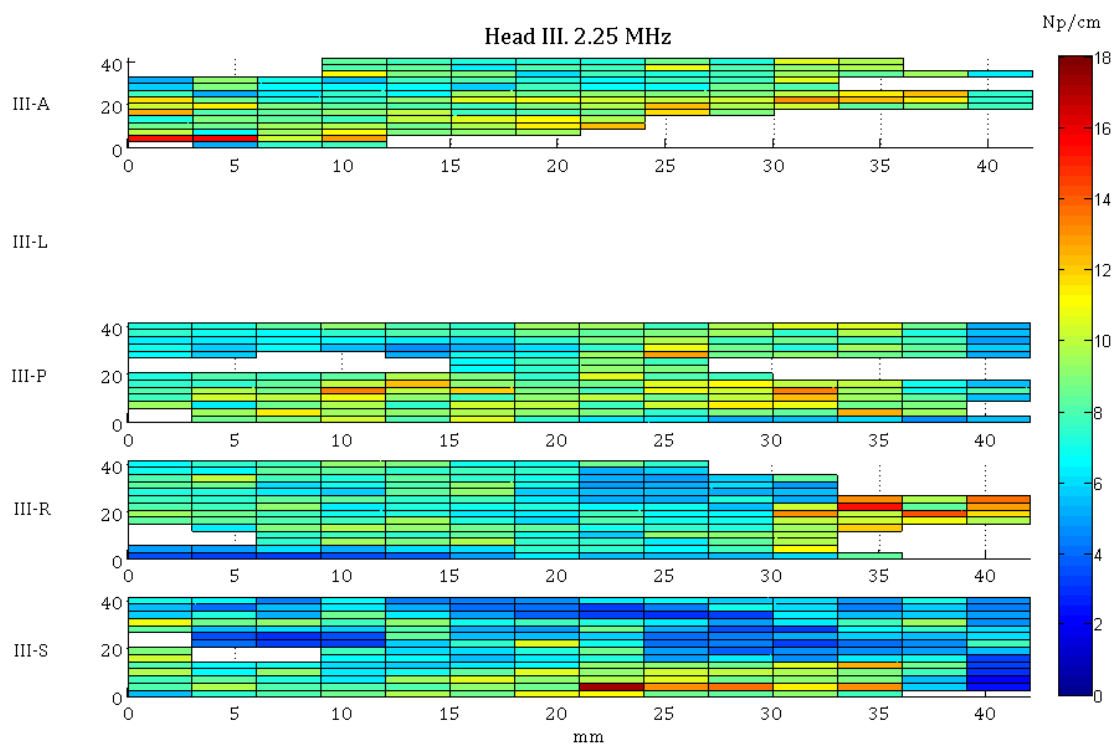
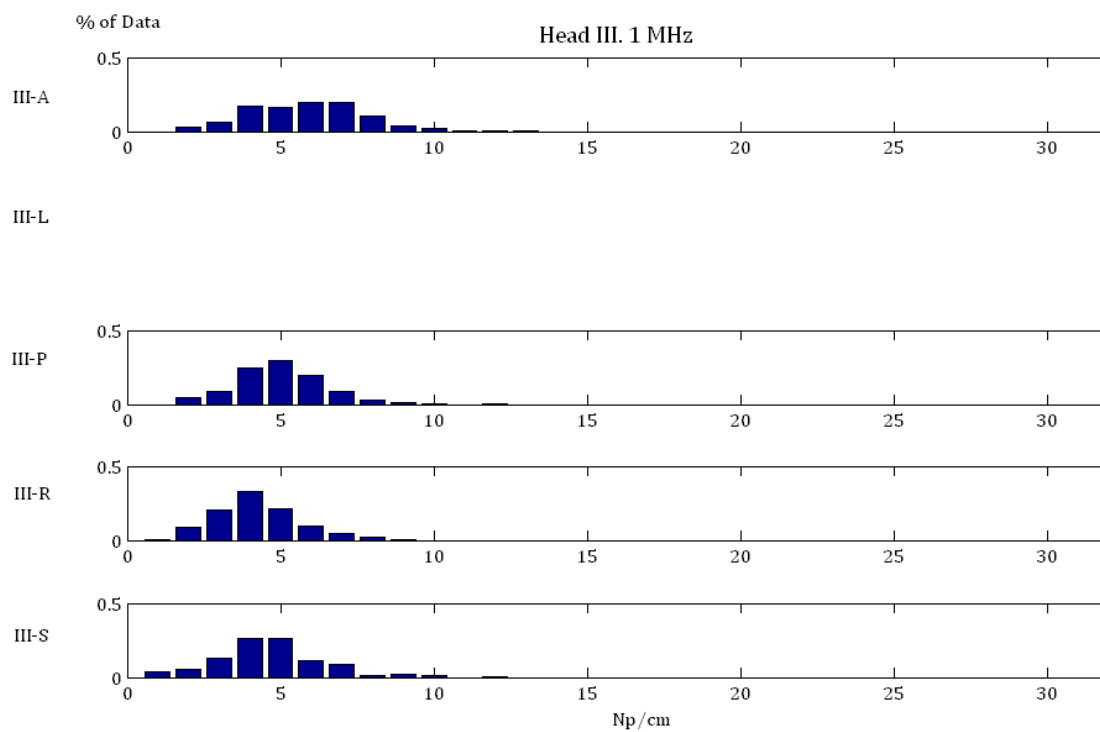


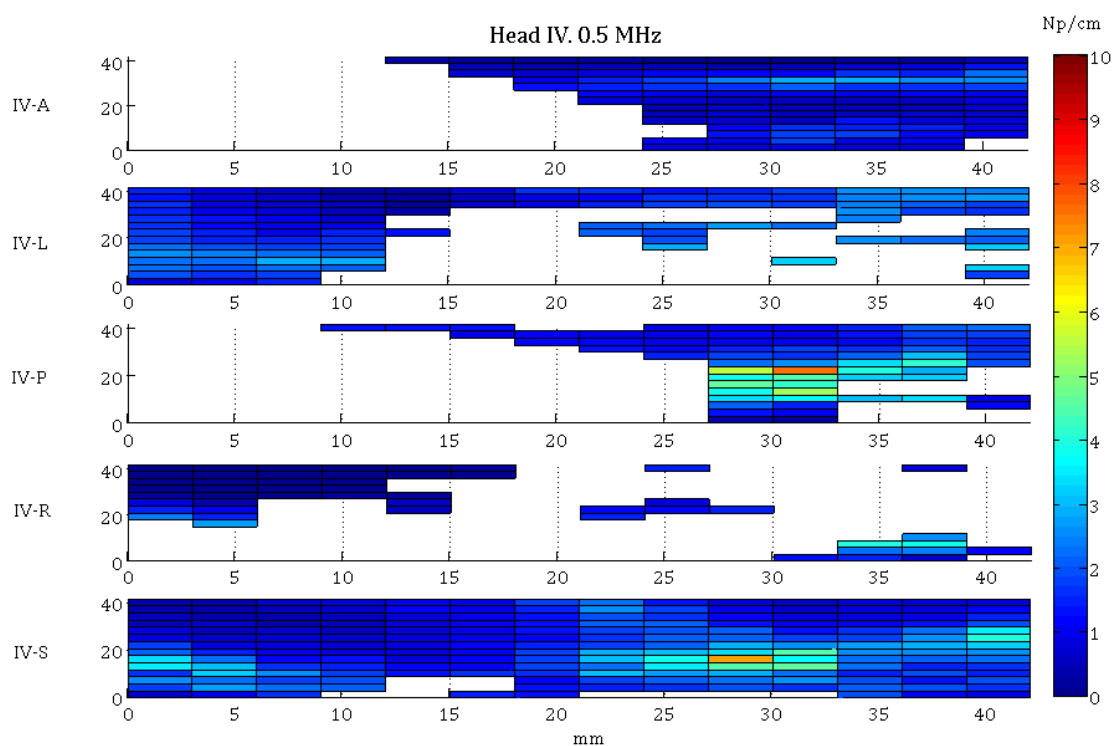
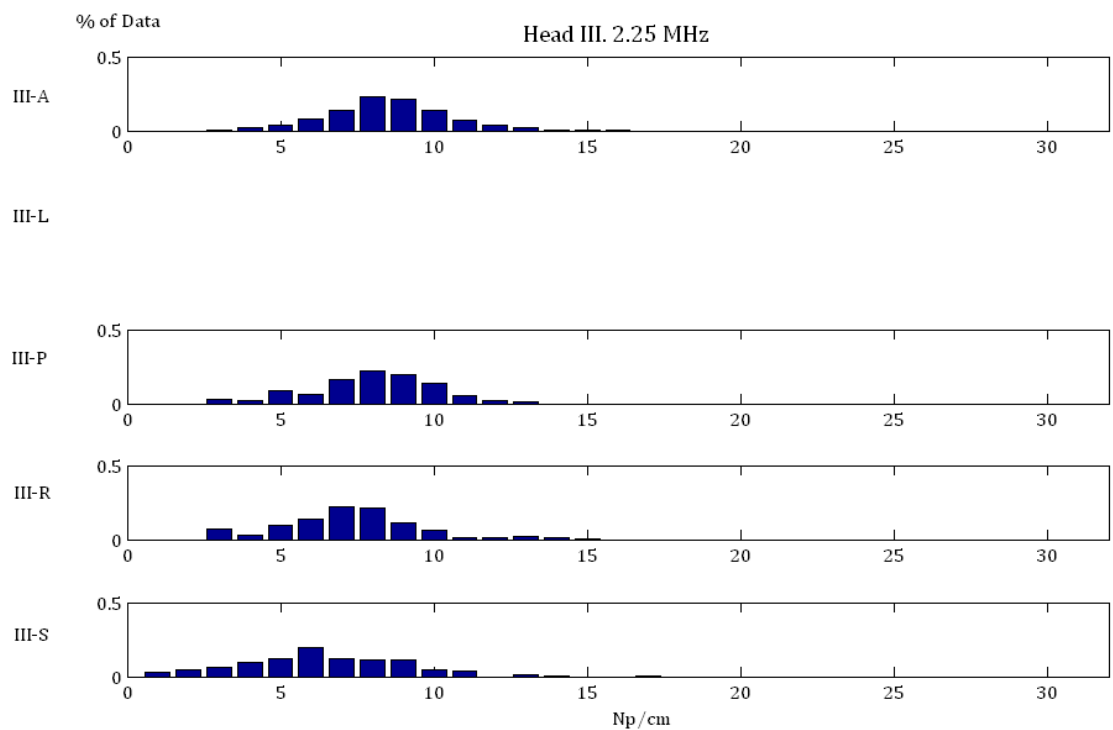


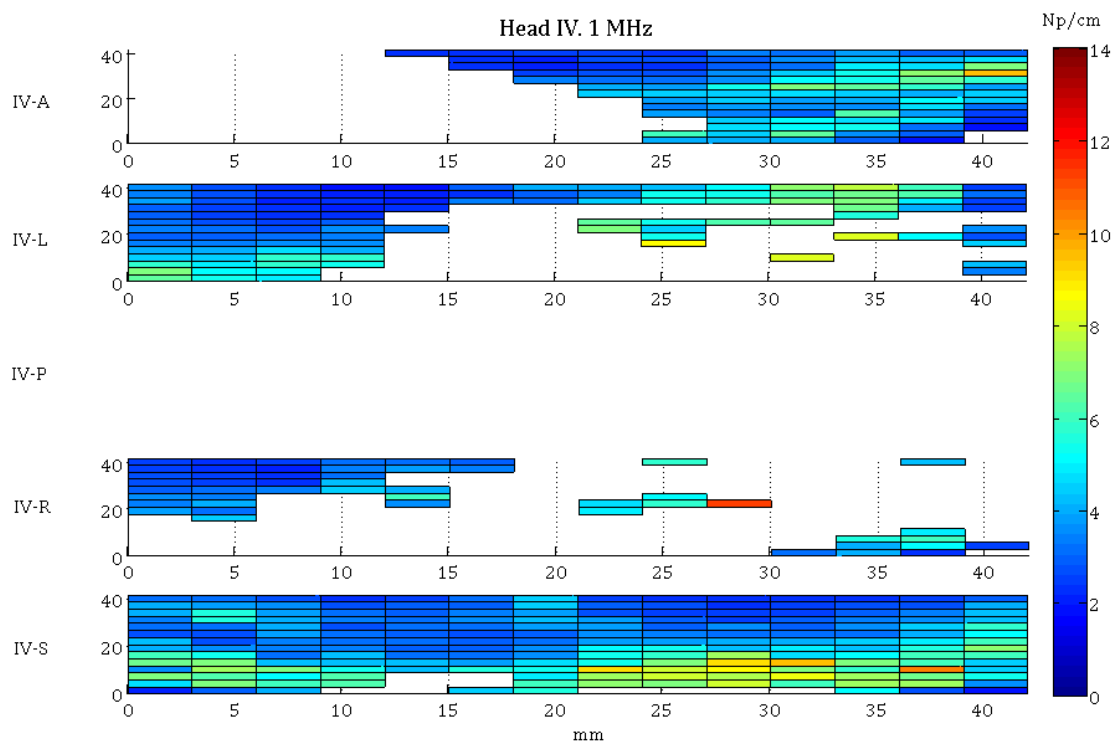
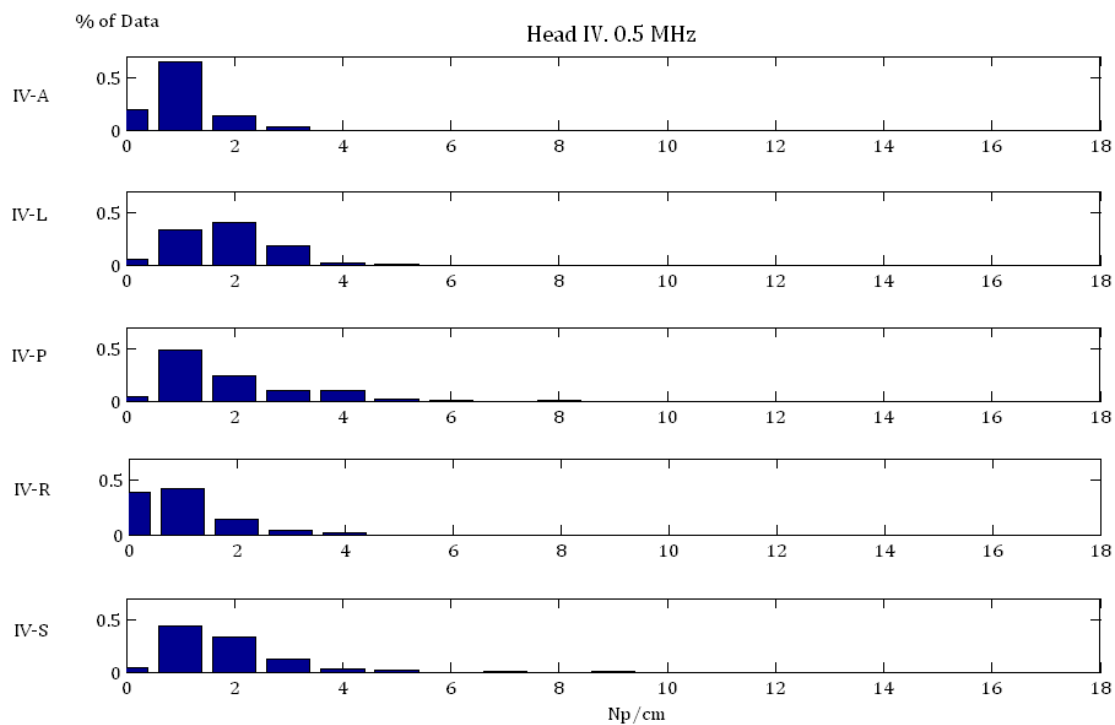


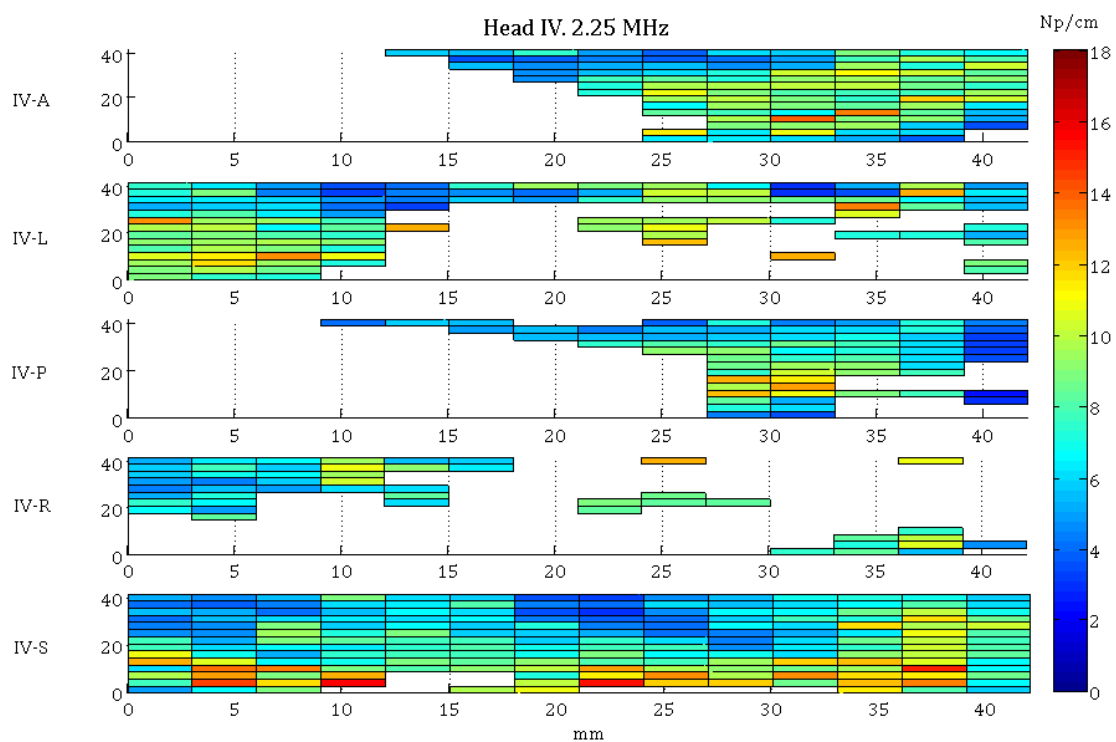
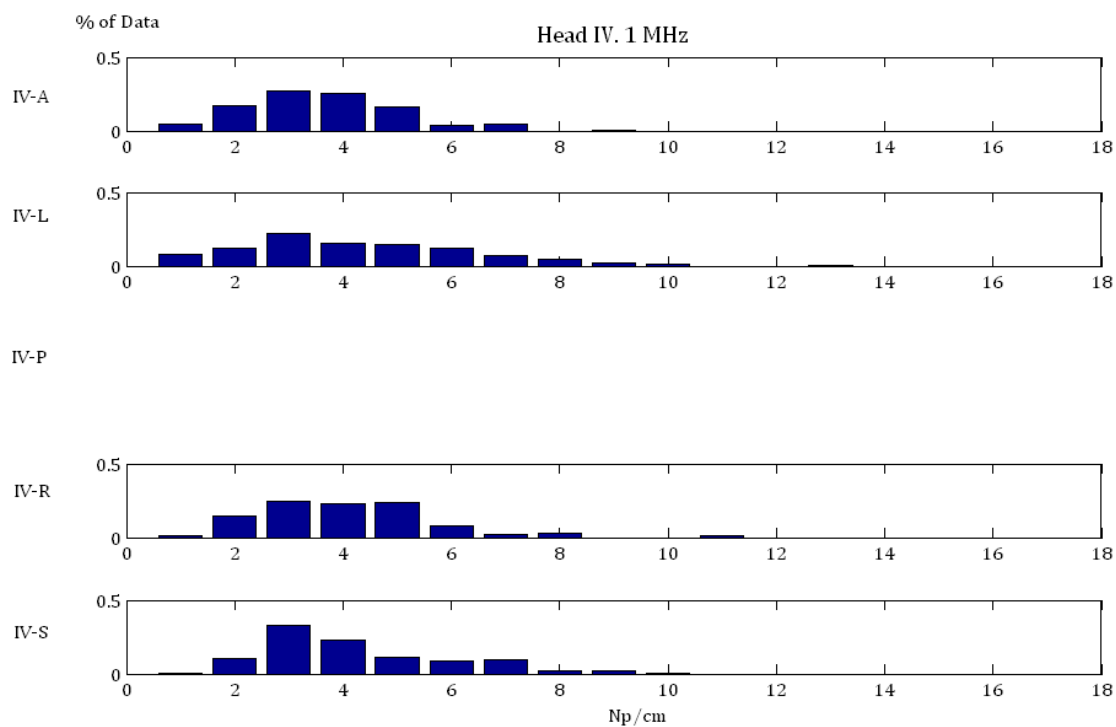


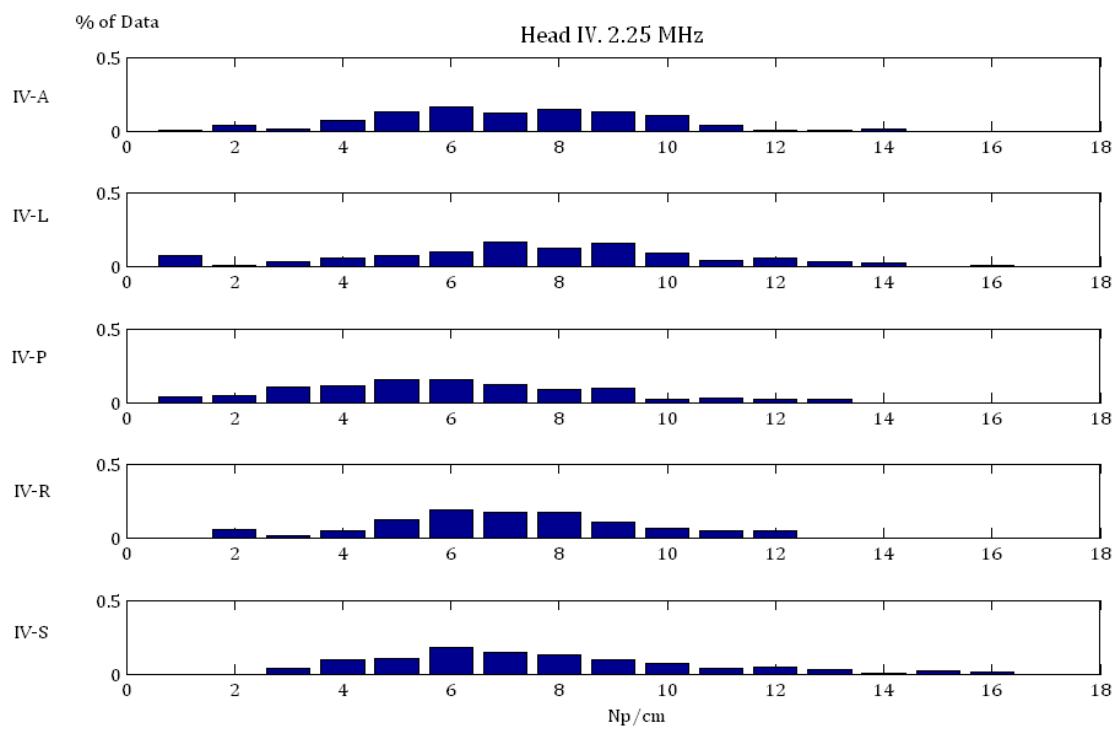














# Appendix C

Results from the t-test performed on the attenuation coefficient mean values for fragments in heads I and IV show higher spatial homogeneity than those obtained for heads II and III. D denotes statistically different and E denotes statistically equal.

			Fragment						
			Equal	I-R			I-S		
			Different	0.5 MHz	1 MHz	2.25 MHz	0.5 MHz	1 MHz	2.25 MHz
Fragment	I-A	0.5 MHz	E			E			
		1 MHz		E			E		
		2.25 MHz			D			D	
	I-R	0.5 MHz				E			
		1 MHz					E		
		2.25 MHz						E	

			Fragment														
			Equal			IV-L			IV-P			IV-R			IV-S		
			Different			0.5 MHz	1 MHz	2.25 MHz	0.5 MHz	1 MHz	2.25 MHz	0.5 MHz	1 MHz	2.25 MHz	0.5 MHz	1 MHz	2.25 MHz
Fragment	IV-A	0.5 MHz	D			D			E			D					
		1 MHz		D						E			D				
		2.25 MHz			E			D			E			E			
	IV-P	0.5 MHz	E						D			E					
		1 MHz															
		2.25 MHz		D							D			D			
	IV-R	0.5 MHz	D			D						D					
		1 MHz		E									E				
		2.25 MHz			E			D						E			
	IV-S	0.5 MHz	E			E			D								
		1 MHz		E						E							
		2.25 MHz			E			D			E						

# Appendix D

Estimation of propagated error for the ultrasonic measurements of thickness, speed of sound, and attenuation coefficient.

For a given calculated property  $R$ , determined from independent measurements such that  $R = R(x_1, x_2, \dots, x_n)$ , and having those measurements uncertainties  $\Delta x_i$ , the total uncertainty for  $R$  can be expressed as,

$$\Delta R = \pm \left[ \sum_1^n \left( \frac{\partial R}{\partial x_i} \Delta x_i \right)^2 \right]^{1/2}.$$

## Thickness

Thickness was calculated using  $D = a + (t_{cc1} - t_{cc2}) \frac{c_w}{2}$ . The uncertainty of this measurement was estimated as follows:

$$\Delta D = \pm \left[ \left( \frac{\partial D}{\partial a} \Delta a \right)^2 + \left( \frac{\partial D}{\partial t_{cc1}} \Delta t_{cc1} \right)^2 + \left( \frac{\partial D}{\partial t_{cc2}} \Delta t_{cc2} \right)^2 + \left( \frac{\partial D}{\partial c_w} \Delta c_w \right)^2 \right]^{1/2},$$

$$\frac{\partial D}{\partial a} = 1,$$

$$\frac{\partial D}{\partial t_{cc1}} = \frac{c_w}{2},$$

$$\frac{\partial D}{\partial t_{cc2}} = -\frac{c_w}{2},$$

$$\frac{\partial D}{\partial c_w} = \frac{t_{cc1} - t_{cc2}}{2},$$

Temperature varied from 15°C to 18°C, therefore  $c_w = 1467 \pm 21 \text{ m/s}$  and  $\Delta c_w = 21 \text{ m/s}$ .

From multiple independent measurements of the reference thickness  $a = 25.09 \text{ mm}$ , a variation of  $\Delta a = 0.12 \text{ mm}$  was recorded.

For an average time delay  $(t_{cc1} - t_{cc2}) = 32\mu s$ , it was assumed an error in the cross-correlation function for echo-pulse signals of half a period. For a 5 MHz wave we have that  $\Delta t_{cci} = 1 * 10^{-7} s$ .

Finally the error for the thickness measurements was estimated to be  $\Delta D = \pm 3.716 * 10^{-4} m$ .

### Speed of sound

Speed of sound was calculated using  $c_b = \frac{D}{\frac{D}{c_w} - |t_{cc}|}$ . Similarly, the uncertainty of this measurement was estimated as follows:

$$\Delta c_b = \pm \left[ \left( \frac{\partial c_b}{\partial D} \Delta D \right)^2 + \left( \frac{\partial c_b}{\partial c_w} \Delta c_w \right)^2 + \left( \frac{\partial c_b}{\partial t_{cc}} \Delta t_{cc} \right)^2 \right]^{1/2},$$

$$\frac{\partial c_b}{\partial D} = - \left[ \frac{1}{\frac{D}{c_w} - |t_{cc}|} + \frac{D}{c_w \left( |t_{cc}| - \frac{D}{c_w} \right)^2} \right],$$

$$\frac{\partial c_b}{\partial c_w} = \left[ \frac{D}{c_w \left( |t_{cc}| - \frac{D}{c_w} \right)} \right]^2,$$

$$\frac{\partial c_b}{\partial t_{cc}} = \frac{D}{\left( |t_{cc}| - \frac{D}{c_w} \right)^2}.$$

In this case for the cross-correlation between through-transmitted pulses, the error was estimated to be a quarter of a period from which it was obtained:

$$\Delta t_{cc}(@0.5MHz) = 5 * 10^{-7} s, \Delta t_{cc}(@1MHz) = 2.5 * 10^{-7} s, \text{ and}$$

$$\Delta t_{cc}(@2.25MHz) = 1.11 * 10^{-7} s.$$

Finally, the estimated errors for the speed of propagated sound at the three

frequencies used were:  $\Delta c_b(@0.5MHz) = \pm 705 m/s$ ,  $\Delta c_b(@1MHz) = \pm 388 m/s$ ,

and  $\Delta c_b(@2.25MHz) = \pm 240 m/s$ .

### Attenuation Coefficient

Attenuation coefficient was determined using  $\alpha = - \left[ \log \left( \frac{A_1(f)}{A_0(f)} \right) + \log(1/T) \right] \frac{1}{D}$ . The

uncertainty of this measurement was estimated as follows:

$$\Delta\alpha = \pm \left[ \left( \frac{\partial\alpha}{\partial A_1} \Delta A_1 \right)^2 + \left( \frac{\partial\alpha}{\partial A_0} \Delta A_0 \right)^2 + \left( \frac{\partial\alpha}{\partial T} \Delta T \right)^2 + \left( \frac{\partial\alpha}{\partial D} \Delta D \right)^2 \right]^{1/2},$$

$$\frac{\partial\alpha}{\partial A_1} = - \frac{1}{A_1 D},$$

$$\frac{\partial\alpha}{\partial A_0} = \frac{1}{A_0 D},$$

$$\frac{\partial\alpha}{\partial T} = \frac{1}{TD},$$

$$\frac{\partial\alpha}{\partial D} = \left[ \log \left( \frac{A_1}{A_0} \right) + \log \left( \frac{1}{T} \right) \right] \frac{1}{D^2}.$$

With the aid of a calibration target, the error in the measurement of the transmitted

pulse through the skull bone was estimated to be:  $\Delta A_1(@0.5MHz) =$

$\pm 0.4 \text{ FFT Amp}$ ,  $\Delta A_1(@1MHz) = \pm 1 \text{ FFT Amp}$ , and  $\Delta A_1(@2.25MHz) =$

$\pm 1.6 \text{ FFT Amp}$

The error in the reference pulse is assumed to be zero.

From the theoretical transmission coefficient curve (see Fig. #), an variation of

$\Delta T = 0.1$  was estimated.

Finally the error in the attenuation coefficients measured at the three frequencies

were:  $\Delta\alpha (@0.5MHz) = \pm 0.30 \text{ Np/cm}$ ,  $\Delta\alpha (@1MHz) = \pm 0.33 \text{ Np/cm}$ , and

$\Delta\alpha (@2.25MHz) = \pm 0.37 \text{ Np/cm}$ .